Journal of
Materials Chemistry A

ROYAL SOCIETY
OF CHEMISTRY

REVIEW

View Article Online
View Journal | View Issue

Cite this: *J. Mater. Chem. A*, 2024, **12**, 33488

High-temperature oxidation behavior of transition metal complex concentrated alloys (TM-CCAs): a comprehensive review

Haofei Sun, Emily Seto, Meifeng Li* and Jing Liu *

Received 27th August 2024
Accepted 25th October 2024

DOI: 10.1039/d4ta06071g

rsc.li/materials-a

The increasing demand for high-efficiency heat engines, along with advancements in the power generation and aerospace industries, necessitates the development of high-temperature (HT) alloys with superior mechanical properties, as well as enhanced oxidation and corrosion resistance. This review comprehensively examines the potential of complex concentrated alloys (CCAs) to meet these demands. Beginning with an overview of the extensively studied Cantor alloy systems, it explores the effects of elemental additions and substitutions-such as Al, Nb, Cu, and Si-on the oxidation behavior of CCAs. The review delves into the mechanisms of oxide scale formation and design strategies for enhancing oxidation resistance. Additionally, it emphasizes the integration of advanced computational techniques and machine learning for alloy development. By synthesizing existing research, this review identifies key knowledge gaps and offers a solid foundation for future CCA research, guiding the intelligent design of next-generation HT alloys.

1. Introduction

The growing demand for higher efficiency in heat engines has continuously elevated the requirements for high-temperature (HT) alloys.[1–3] In the power generation industry, including nuclear, coal-fired, and oil-fired, increasing operating temperatures contribute to reduced fuel consumption, decreased pollution, and lower operating costs.[4–6] Similarly, higher operating temperatures in jet engines in the aerospace industry enhance performance, allowing for heavier payloads, greater speed, and extended range.[7–9] Such material requirements have initiated a revolution in materials science, favoring the use of alloys over pure metals. Specifically, the development of new HT alloys faces the challenge of balancing low component costs with superior HT performance.[10] This has led to research efforts aimed at developing new categories of materials that are lightweight, cost-effective, possess superior HT mechanical properties, and demonstrate high resistance to oxidation and corrosion.[11,12]

Complex concentrated alloys (CCAs) have emerged as a promising solution, balancing performance and economic efficiency.[13,14] Initially developed by Cantor and Yeh *et al.*, the concept of CCAs introduced a new equiatomic CCA FeCrNiCoMn (also known as the Cantor alloy) with a single face-centered cubic (FCC) structure.[15,16] CCAs, also referred to as high/medium-entropy alloys (HEAs/MEAs), typically consist of multiple main alloying elements (generally 3–5), leading to a high mixing entropy (ΔS_{mix}). In comparison, traditional alloys have a low ΔS_{mix} (less than 1R) and are typically composed of one or two main elements. Due to the entropy effect, instead of precipitating intermetallic and complex phases, CCAs tend to form simple structural phases such as FCC,[17,18] body-centered cubic (BCC),[19,20] and close-packed hexagonal (HCP).[21,22] This simplicity in structure allows CCAs to exhibit properties that exceed the mere combinations of their constituent elements. CCAs have demonstrated many unique properties, including high strength, high ductility,[23,24] superior thermal stability,[25,26] substantial oxidation behavior,[27,28] and resistance to oxidation/corrosion.[29,30]

CCAs can be classified by elemental composition into either transition metal (TM)-CCAs or refractory (R)-CCAs. TM-CCAs, especially Cantor alloys, are often used as prototype models and have been extensively developed by adding, modifying, or replacing elements to improve performance in extremely harsh environments, such as those found in nuclear, marine engineering, and aerospace industries,[31–33] where a high risk of mechanical failure and HT oxidation is significant. The mechanical properties of HEAs/CCAs have been summarized and reviewed by George *et al.*[34] Most compressive data at room temperature show ultimate compressive strength values ranging from 1000 to 2300 MPa and strain values between 0.1–15%, indicating significantly enhanced compressive properties compared to those of conventionally engineered alloys. For instance, the $\text{FeCrNiCoAl}_{0.3}$ HEA is reported to exhibit a compressive strain of 97% and a compressive strength of 1378 MPa.[35] An ultra-high compressive strength of 4390 MPa has been reported for the FeCrNiCoAl HEA at ambient

---

Department of Chemical and Materials Engineering, University of Alberta, Edmonton, Alberta T6G 1H9, Canada. E-mail: meifeng1@ualberta.ca; jing.liu.arrow@ualberta.ca

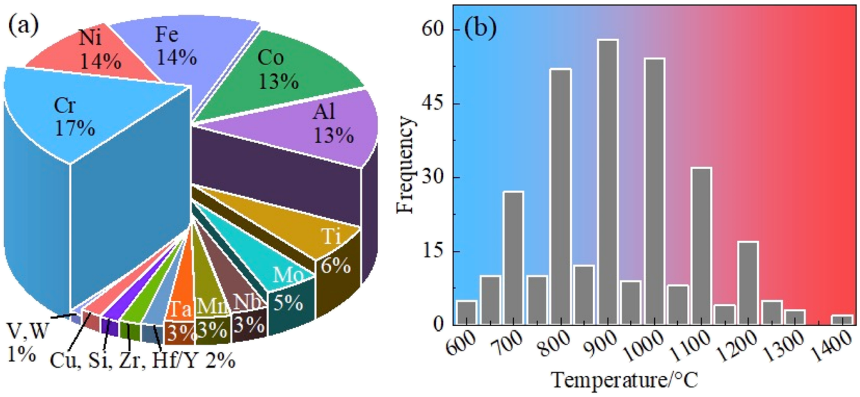

Fig. 1 Commonly used elements and their occurrence frequency in CCA development (a) and the count of occurrence frequency for each testing temperature of CCAs (b) (data from Appendix Tables 1–5 covering the years 2004 to 2024).

temperature.[36] However, the specific strengths of the surveyed HEAs drop significantly at temperatures above 600 °C.[34] Notably, the simultaneous alloying of Al and Ti, combined with short-term annealing treatment, leads to an exception with superior specific strength values.[37] On the other hand, the addition of Al, Cu, and Ni does not significantly contribute to strength enhancement.[38,39] The compositional flexibility offered by the multi-element space allows for the exploration of multiple mechanisms, which may lead to new alloys with superior mechanical properties compared to current engineering alloys.

A review of publications from 2004 to 2024 on CCAs used for HT oxidation was conducted and the most common elements in CCAs for oxidation tests are shown in Fig. 1a, where elemental proportion is defined as the frequency of each element occurring in alloys relative to the total number of elements. TM elements Cr, Ni, Fe, Co, and post-TM element Al are the most popular with frequencies higher than 10%. Additionally, refractory elements such as Ti, Mo, and Nb are commonly used with low frequencies (around 5%). The restriction of R-CCA application can be explained by the difficult preparation process for R-CCAs due to high melting points and high room temperature (RT) brittleness.[40] Fig. 1b displays the frequency of testing temperatures, defined as the number of occurrences of each testing temperature within the reviewed publications. It reveals that the most common oxidation testing temperatures for CCAs mainly range around 800 °C, 900 °C, and 1000 °C, which fits the service temperatures of engine applications.

This work reviews research papers on the HT oxidation of TM-CCAs focusing on the application of oxidation data and identifying gaps for future research. It begins with an overview of the operating/testing temperatures and commonly used elements in CCAs, providing a context for understanding their performance under HT conditions. Then, the review delves into the oxidation behavior of Cantor alloy systems and other TM MEA systems, examining the effects of various alloying elements on oxidation resistance. Finally, the knowledge gaps requiring further investigation are identified, aiming to highlight areas where future research should be directed. The goal of this study is to provide a comprehensive review of the literature, effectively communicating existing oxidation data and identifying the remaining research gaps. It establishes a solid foundation for future CCA design and highlights the potential of machine learning (ML) for the prediction of their oxidation resistance from a data-oriented perspective.

2. Cantor alloy system

2.1. Fe–Cr–Ni–Co–Mn system

The FCC FeCrNiCoMn system, commonly known as the Cantor alloy, first proposed by Cantor and Yeh *et al.* in 2004, is one of the most extensively studied HEAs.[15,16] Significant oxidation data exists for equiatomic FeCrNiCoMn, summarized in Appendix Table 1. Fig. 2a illustrates selected oxidation data for FeCrNiCoMn at temperatures ranging from 800 °C to 1000 °C. The mass gain curves of FeCrNiCoMn, from various methods such as vacuum induction melting (IM),[43,47] arc-melting (AM),[41,42,44,45,48] and vacuum gas atomization,[49] exhibit similar trends at the same temperature.

Studying the phase stability and possible transformations is critical for designing CCAs with optimal material properties.[50,51] In this study, the predicted HT stable phase structures were calculated using the software Thermo-Calc (Database HEA 6.1), with the results shown in Appendix Table 1 and Appendix Fig. 14. The alloys in the Fe–Cr–Ni–Co–Mn system with different Fe contents contain the sigma phase below 850 °C (Appendix Fig. 14a) and show a high proportion at lower temperatures (31% at 600 °C, 19% at 700 °C and 4% at 800 °C). This sigma phase can weaken the corrosion resistance and cause embrittlement failure.[52,53] Therefore, such alloys should be avoided for use under 850 °C to prevent sigma phase formation and its consequent effects.

As detailed in Appendix Table 1, after 24 hours, the parabolic rate constant k_w (with the unit of mg^2 cm^{-4} h^{-1}) of FeCrNiCoMn, calculated by Adomako *et al.*, is 3.41×10^{-4} at 800 °C, 1.27×10^{-3} at 900 °C, and 0.012 at 1000 °C.[41] After 48 hours, k_w values calculated by Kai *et al.* are 0.054 and 0.104 mg^2 cm^{-4} h^{-1} at 800 °C and 900 °C, respectively.[44] For 100 hours, k_w values are

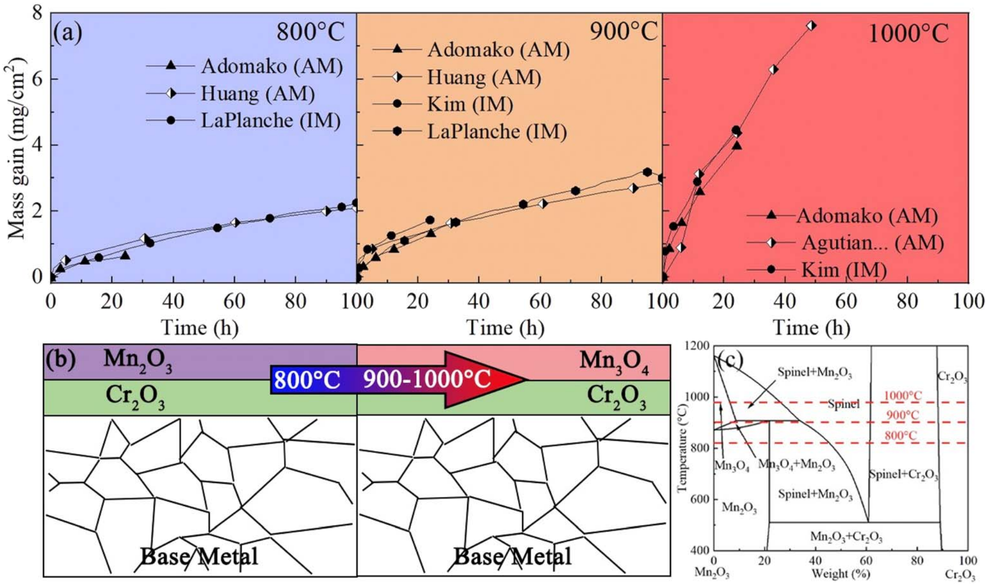

Fig. 2 Mass gain curves of the equiatomic FeCrNiCoMn alloy during oxidation at 800–1000 °C, with arc-melting noted as AM and induction melting noted as IM (a); schematics of thermally grown oxide (TGO) layer formation (b); and the phase diagram of Mn_2O_3–Cr_2O_3 (c) (curve data adapted from Adomako,[41] Huang,[42] LaPlanche,[43] Kim,[44] and Agustianingrum,[45] and phase diagram from ref. 46).

0.18 and 1.347 mg^2 cm^{-4} h^{-1} at 900 °C and 1000 °C, respectively.[45] Notably, the increase in k_w from 900 °C to 1000 °C (around 8 to 10 times higher) is much more significant than from 800 °C and 900 °C (around 2 to 4 times higher). The data and curves in Fig. 2a indicate rapid mass gain above 1000 °C, as reflected by the higher k_w values at this temperature compared to that from 800 °C and 900 °C.

To further understand the oxidation mechanism, many studies have been conducted to analyze the oxide scale. Fig. 2b displays the distributions of oxidation layers. At 800 °C, the outer layer comprises Mn_2O_3 with an inner layer of Cr_2O_3. As the temperature rises to 900 °C, the outer layer transitions to Mn_3O_4, which can be explained using the Mn oxide–Cr_2O_3 phase diagram (Fig. 2c).[46] More specifically, Mn_2O_3 is stable and can incorporate up to 21 wt% Cr in solid solutions below 850 °C, whereas Mn_3O_4 is stable between 850 °C and 1150 °C and can incorporate up to 8 wt% Cr in the solid solution (Fig. 2c).[54,55] At 1000 °C, Mn_3O_4 and Cr_2O_3 form a mixed layer,[41] as concentrations of Mn and Cr increase and they are dispersed throughout the oxide layer due to their increased diffusion rate at higher temperatures. The predominance of the Mn-rich outer layer (Mn_2O_3/Mn_3O_4) suggests that Mn diffuses faster than Cr.[43] This is supported by the observation that Mn exhibits the highest diffusivity and the lowest activation energy of diffusion in the Fe–Cr–Ni–Co–Mn system.[56]

Researchers have begun tailoring the elemental ratio in the Fe–Cr–Ni–Co–Mn system.[45,57] For instance, the oxidation behavior of $Fe_x(CrNiCoMn)_{100-x}$, including Fe20, Fe40, and Fe60, indicates that the oxidation rate increases with higher Fe content.[45] As shown in Fig. 3a, the mass gains of Fe20 and Fe40 after 48 hours are relatively similar, while Fe60 shows a significant increase in the mass gain, suggesting that alloys with higher Fe content are more susceptible to oxidation. The mass gain curves at 1100 °C (Fig. 3b) demonstrate that Fe60 exhibits the highest periodically increased mass gain. Schematics in Fig. 3c illustrate the distribution of oxidation layers. Cr_2O_3 forms as the inner layer on the surface of the Fe20 and Fe40 due to the high oxygen affinity of Cr, which requires a relatively low oxygen partial pressure at the front of the oxidation zone.[41] In Fe60, Cr is enriched at the grain boundaries due to internal oxidation, and the Cr content on the surface is insufficient to create a stable Cr_2O_3 layer (Fig. 3d). Mn_3O_4 is found as the outer layer, with Fe_3O_4 mixed on top due to the high diffusivity of Fe. The rapid outward diffusion of Mn and Cr creates vacancies in the alloys, which later coalesce into Kirkendall voids,[58] leading to a porous zone at the interface between the oxide and base alloy.

2.2. Fe–Cr–Ni–Co–Mn + M sub-system

The distinct combination and number of constituent elements in CCAs significantly influence the nature and continuity of the evolved oxide scale and, therefore, affect the HT oxidation resistance of these alloys. Incorporating additional elements into the original system can enhance the oxidation resistance of the Fe–Cr–Ni–Co–Mn + M system (M = Al, Nb, *etc.*). For instance, adding various amounts of Al leads to a noticeable decrease in the mass gain during the oxidation of $(FeCoCrNiMn)_{100-x}Al_x$ alloys (referred to as Al_x alloys) over 100 hours at 900 °C (Fig. 4a).[48] Specifically, the mass gain reduces from 1.51 mg cm^{-2} for Al_{10} alloy to 1.08 mg cm^{-2} for Al_{29} alloy. This reduction is primarily due to the increased formation of an Al_2O_3 protective layer for the alloy with higher Al content, resulting in a flatter and denser oxide layer surface. After 100 hours of oxidation, the Al_2O_3 layer thickens while the overall

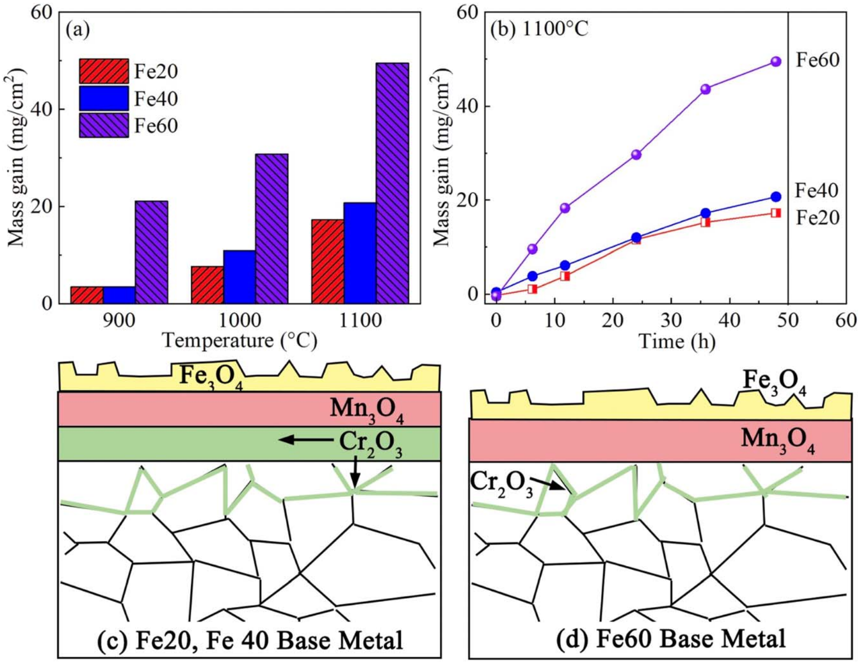

Fig. 3 Mass gain of Fe$_x$(CrNiCoMn)$_{(100-x)}$ alloys after 48 hours of oxidation at 900 °C, 1000 °C, and 1100 °C (a); mass gain curves of these alloys during oxidation at 1100 °C (b); and schematics showing the distribution of the TGO layer with varying Fe content at 1100 °C (c and d).[45]

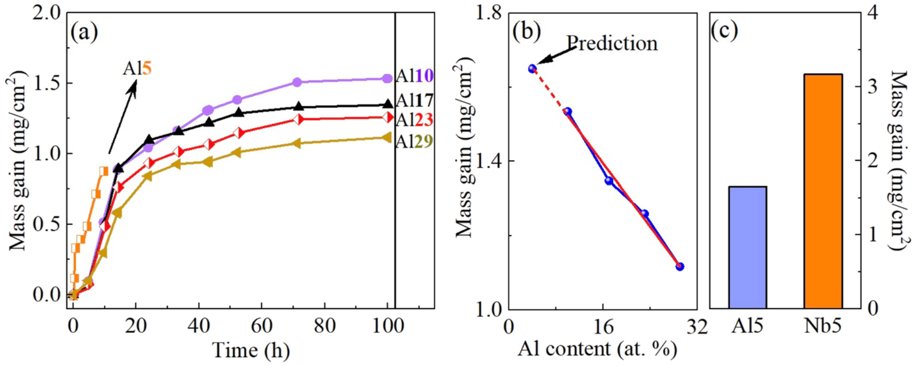

Fig. 4 Mass gain curves of (FeCoCrNiMn)$_{95}$Al$_5$ (Al5)[59] to (FeCoCrNiMn)$_{71}$Al$_{29}$ (Al29)[48] during oxidation at 900 °C (a); the relationship between Al content and mass gain after 100 hour oxidation at 900 °C (b); and the mass gain of Al5 (predicted) and (FeCoCrNiMn)$_{95}$Nb$_5$ (Nb5) alloys after 100 hour oxidation at 900 °C (ref. 42) (c).

oxide layer thickness diminishes, suggesting that Al$_2$O$_3$ effectively inhibits the inward diffusion of oxygen, thereby slowing the oxidation process and enhancing the HT oxidation resistance of the cladding layer.[48]

The HT oxidation process includes two stages: an initial rapid oxidation stage within the first 10 hours and a subsequent steady-state oxidation stage. To provide a detailed description of the oxidation kinetics, Ye *et al.* calculated the k_w separately for the intervals from 0–10 and 10–100 hours.[48] As detailed in Appendix Table 2, during the initial 0–10 hours, k_w values are approximately 1.2×10^{-4} mg^2 cm^{-4} h^{-1} for Al$_{10}$ and Al$_{17}$, and around 4–8 $\times 10^{-5}$ mg^2 cm^{-4} h^{-1} for Al$_{23}$ and Al$_{29}$. During the subsequent 10–100 hours, k_w for these four alloys remains consistent, around 2–3 $\times 10^{-6}$ mg^2 cm^{-4} h^{-1}. This highlights the importance of the test duration on the oxidation data, as the steady-state stage appears to exhibit similar k_w values. Notably, when oxidized for only 10 hours, the Al$_5$ alloy does not reach the steady-state stage of the mass gain curve.[59] Therefore, by extrapolating from the linear relationship of mass gain after 100 hours with Al content ranging from 10% to 29%, the estimated mass gain of the Al$_5$ alloy after 100 hours is around 1.5 mg cm^{-2}, as illustrated in Fig. 4b. The predicted mass gain is two times lower than that of (FeCoCrNiMn)$_{95}$Nb$_5$ (named Nb$_5$) under the same condition, which is around 3.2 mg cm^{-2}, as shown in Fig. 4c. This indicates that Nb does not significantly improve the oxidation resistance.[42] The addition of Nb$_5$ leads to the

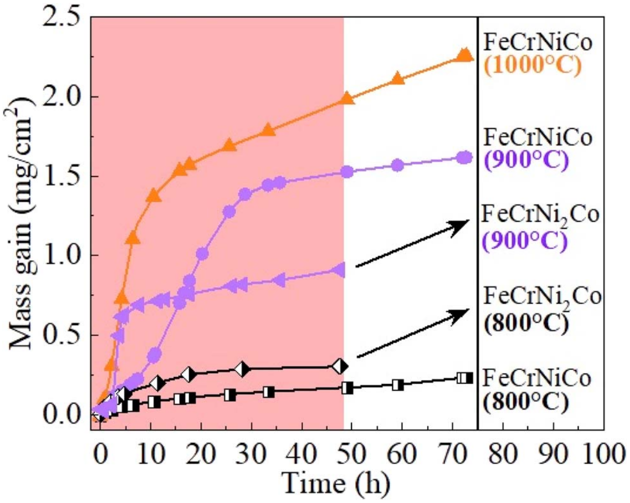

Fig. 5 Mass gain curves of Fe–Cr–Ni–Co alloys during oxidation at various temperatures (data from FeCrNiCo[60] and FeCrNi$_2$Co[61]).

formation of an Nb-rich Laves intermetallic phase layer on the alloy surface. However, the Laves phase layer fails to prevent internal oxidation and even becomes a channel for the inward diffusion of oxygen.[42] According to our phase structure calculation, the formation of the Laves phase aligns with the predicted phase fraction of around 13–17 vol% at this temperature range. This provides valuable insights into designing HT alloys to avoid this phase.

2.3. Fe–Cr–Ni–Co system

Given that Mn oxides are known to be non-protective, the FeCrNiCo system has been further investigated after removing Mn. As illustrated in Fig. 5, increasing Ni content from 25 at% in FeCrNiCo[60] to 40 at% in FeCrNi$_2$Co[61] results in varying oxidation behaviours at different temperatures. At 800 °C, the increased Ni content raises the mass gain from 0.17 to 0.30 mg cm^{-2}, while at 900 °C, higher Ni content results in a decreased mass gain from 1.52 to 0.91 mg cm^{-2}. The two alloys show similar distributions of the oxide layers, with a spinel structure ($FeCr_2O_4$ and $NiCo_2O_4$) forming as an outer layer and Cr_2O_3 as an inner layer. The thickness of the inner protective Cr_2O_3 layer in FeCrNi$_2$Co increases significantly as the temperature rises,[61] which leads to the decreased mass gain at 900 °C. Another long-term test demonstrates that FeCrNiCo maintains the same oxidation layer distribution even after 500 hours, with a steady increase in the mass gain.[62] Moreover, according to the phase calculation results shown in Appendix Table 3, both alloys indicate a single FCC phase across the tested temperature

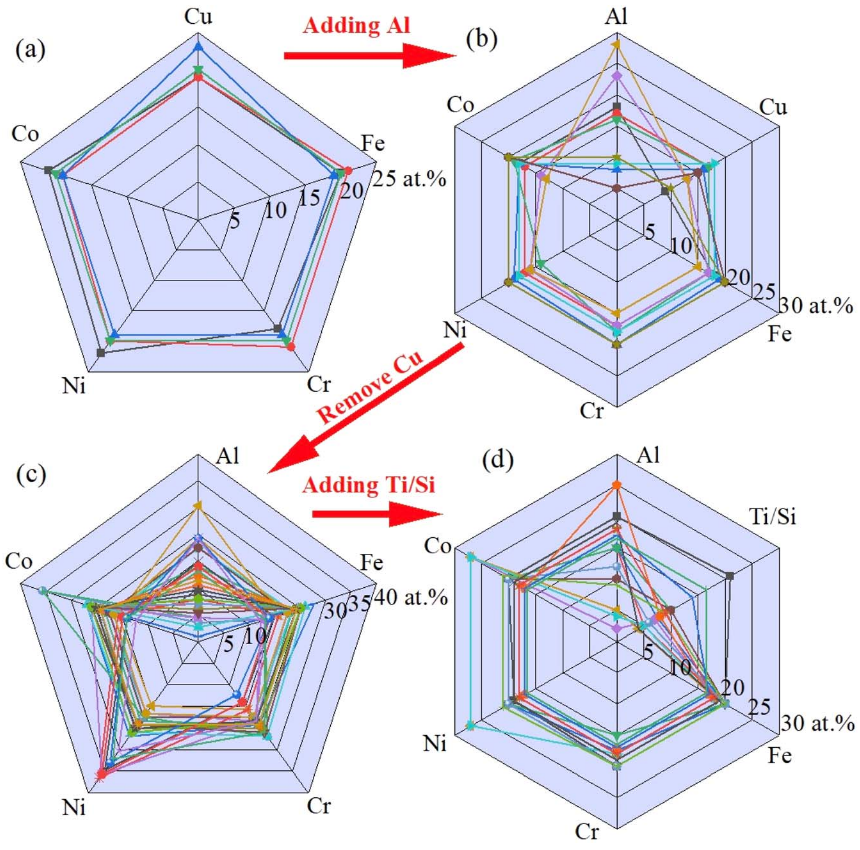

Fig. 6 Fe–Cr–Ni–Co-M sub-systems: (a) FeCrNiCoCu systems, (b) FeCrNiCoCuAl systems, (c) FeCrNiCoAl systems, and (d) FeCrNiCoAlTi/Si systems (data from Appendix Table 4).

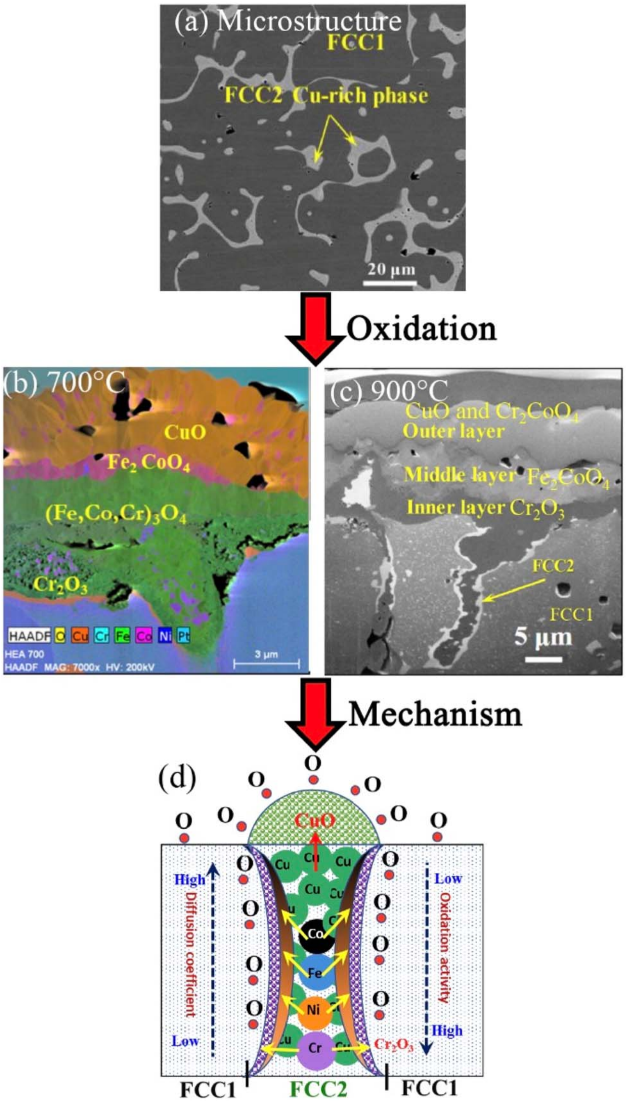

Fig. 7 Microstructure (a), cross-sectional morphologies after 100 hours of oxidation at 700 °C (b) and 900 °C (c), and oxidation mechanisms (d) of the FeCrNiCoCu alloy[66] (reproduced from ref. 66 with permission from [Elsevier], copyright [2022]).

range, indicating a simple phase structure. In Appendix Fig. 16, alloys with varying Fe or Co contents show a single FCC structure above 900 °C, and to maintain this phase structure the Cr content should be limited to below 40 at%.

In summary, while removing Mn and increasing the Ni content in the FeCrNiCo system alters the oxidation behavior, the formation of a thicker Cr_2O_3 protective layer at higher temperatures improves the oxidation resistance, particularly at 900 °C. This suggests that optimizing the Ni content in the FeCrNiCo system can significantly enhance its HT oxidation resistance.

2.4. Fe–Cr–Ni–Co + M system

Building upon insights from Section 2.3, FeCrNiCo CCAs generally exhibit a single FCC structure, which can lead to limited strength. To address this, additional elements such as Cu, Al, Ti, Si, Nb, and B, have been added to balance the strength and plasticity, as well as enhance the oxidation and corrosion resistance.[63,64] Fig. 6 summarizes an overview of the most investigated Fe–Cr–Ni–Co + M systems.

Cu-containing CCAs like FeCrNiCoCu promote the formation of two distinct FCC phases: a primary ductile FCC1 phase and a secondary Cu-rich FCC2 phase,[65] as shown in the back-scattered electron (BSE) image of Fig. 7a. The secondary Cu-rich FCC phase acts as a hardening network, enhancing the strength of the matrix, and slightly improving ductility in comparison to FeCrNiCo.[67] Additionally, the Al addition has been noted to improve Young's modulus, hardness, and yield strength of FeCrNiCoCuAl. The $(FeCrNiCo)_{0.75}Cu_{0.5}$ alloy, for instance, demonstrates outstanding comprehensive mechanical properties with a fracture strength of 2270 MPa and a plastic strain of 43%.[63] Moreover, the oxidation resistance of CCAs plays a crucial role in the serviceability of structural materials.

Recent studies have also explored the effects of replacing Cu with Al on the oxidation behavior of CCAs (Fig. 6a–c). After 100 hours of oxidation at 700 °C, the FeCrNiCoCu alloy forms a loose outer layer of CuO, internal oxides of Fe, Co, and Ni, and a thin Cr_2O_3 layer as the inner layer, as confirmed by SEM/EDS analysis (Fig. 7b).[66] Increasing the temperature to 900 °C results in a predominantly pure and thick Cr_2O_3 inner layer, which extends into the matrix through the FCC2 network (Fig. 7c). This layer formation mechanism involves the interplay of oxidation activity and diffusion rates. It is known that a lower equilibrium partial pressure of oxygen ($\ln p_{O_2}$) indicates higher oxidation activity. For example, the $\ln p_{O_2}$ of Cr–Cr_2O_3 co-existence is lower than that of Fe, Co, Ni and Cu, indicating that Cr exhibits high oxidation activity.[68] The diffusivity can be reflected by diffusion coefficient D through density functional theory (DFT), calculations. In the FeCrNiCoCu alloy, calculation[66] and measured data[69] show that the diffusivity of metal elements (D^{M}) follows the order of $D^{Cu} > D^{Fe} > D^{Co} > D^{Cr} > D^{Ni}$ in the FCC1 phase. D^{M} follows the same order in FCC2 but with significantly higher values. The high oxidation activity of Cr and high diffusivity of Cu leads to a fast-growth outer layer of CuO and a slow-growing Cr-rich inner layer (Fig. 7d).

In TM HEAs, the diffusivities of O and selected constituents (Cu, Cr, and Al) are summarized, as these are the main compositions of the as-grown oxide scales.[66] As shown in Fig. 8a, the diffusivity of O (D^{O}) presents a descending order of FCC2-FeCrNiCo($Cu_{15}Al_5$) > BCC-FeCrNiCo($Cu_{10}Al_{10}$) > FCC2–FeCrNiCoCu > FCC1-FeCrNiCoCu > FCC1-FeCrNiCo($Cu_{15}Al_5$), indicating that the O diffuses faster in FCC2 than in FCC1. Similarly, D^{Cu} of FCC2 phases is the highest (Fig. 8b), following a descending order in FCC2-FeCrNiCoCu > FCC2-

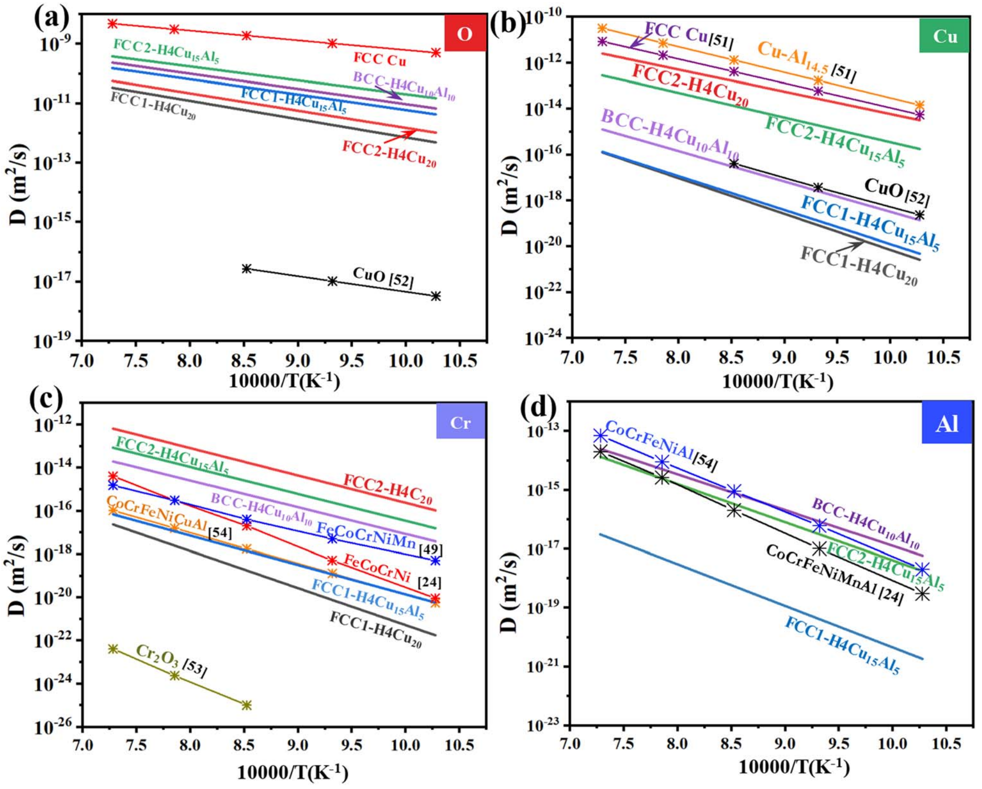

Fig. 8 Comparison of the temperature-dependent D of (a) O, (b) Cu, (c) Cr, and (d) Al in various phases of TM HEAs[66] (reproduced from ref. 66 with permission from [Elsevier], copyright [2022]).

FeCrNiCo($Cu_{15}Al_5$) > BCC-FeCrNiCo($Cu_{10}Al_{10}$) > CuO[70] > FCC1-FeCrNiCoCu > FCC1-FeCrNiCo($Cu_{15}Al_5$). Fig. 8c indicates that the D^{Cr} is generally larger in FCC2 phases than in FCC1 phases, and is significantly lower in Cr_2O_3.[71] D^{Al} shows similar behavior to Cr, *i.e.*, generally faster in FCC2 phases than in FCC1 phases, and this trend increases with increasing Al content in phases.

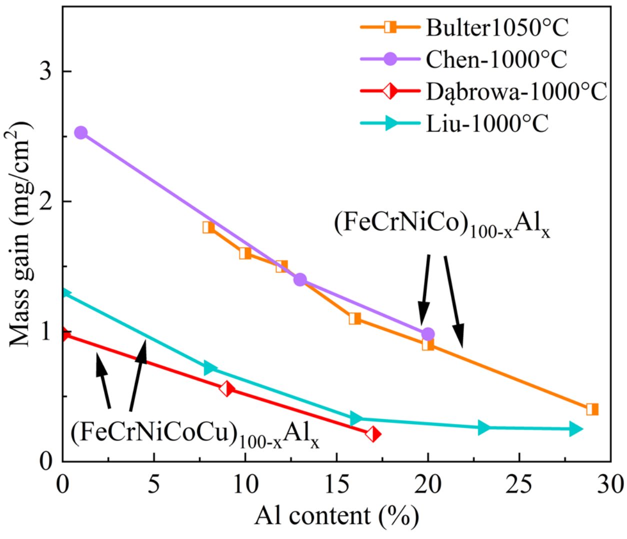

Fig. 9 Mass gain after 100 hours of oxidation with varying Al content in FeCrNiCoCuAl systems (data from Butler,[73,74] Chen,[75] Dąbrowa,[65] and Liu[72]).

According to the results, diffusion in the examined high-entropy phases (HEPs) is generally slower than in low/medium-entropy phases (LEPs/MEPS) with the same constituents. For example, BCC-FeCrNiCo($Cu_{10}Al_{10}$) HEP shows high diffusion rates, which can be attributed to the less dense-packed structure of the BCC phase (compared to the FCC phase), and strong dependence on the individual constituent. Therefore, one cannot simply assume slow diffusion in HE systems based solely on the increase in the number of constituent element types; the specific types of constituent elements and phase structure also play more pronounced roles.

The beneficial effect of Al on the oxidation resistance was evaluated based on the quality of the oxidation scale and oxidation rate of CCAs.[72] Varying Al content added to FeCoCrNiCu has been investigated, as shown in Fig. 7b. Results after 100 hours of oxidation are plotted in Fig. 9 and indicate that increasing Al content enhances oxidation resistance through the formation of an Al_2O_3 layer. However, Cu addition in the FeCrNiCoCuAl system results in poor adhesion of the Al_2O_3 oxide scale to the alloy surface. As reported, the CuO outer layer tends to detach from the substrate after 30 min of oxidation between 1000 °C and 1250 °C.[76] In contrast, increasing the Al content improves oxidation resistance by forming pure or Al-rich oxide scales.[65,72] Consequently, Cu has been systematically removed from the HT CCAs system, as shown in Fig. 6b and c. Meanwhile, comparing FeCrNiCoAl with FeCrNiCoCuAl for the same Al content (Fig. 9) shows that mass gain increases for the FeCrNiCoAl alloy,[73,75,77] indicating poorer oxidation resistance.

Small additions of Si have beneficial effects on oxidation resistance. Si addition improves oxidation resistance by forming a continuous SiO_2 layer at the alloy/scale interface.[78] Comparisons between $Fe_{22}Cr_{22}Ni_{22}Co_{22}Al_{13}$ and $Fe_{20}Cr_{20}Ni_{20}Co_{20}Al_{12}Si_6$ indicate that the Si addition positively affects oxidation resistance at 800 °C but has a negative impact on oxidation resistance at 900–1000 °C.[75] Adding Si promotes the formation of a continuous Al_2O_3 layer at 800 °C and prevents the formation of AlN at this temperature. To further reveal the effect of Si, investigations on adding various Si contents from 0 to 16.5 at% show that $Fe_{19}Cr_{19}Ni_{19}Co_{19}Al_{19}Si_4$ offers the best oxidation resistance as the Si contributes to the formation of a single, compact Al_2O_3 scale.[79] Furthermore, after oxidation, $Fe_{20}Cr_{20}Ni_{20}Co_{20}Si_{20}$ and $Fe_{20}Cr_{20}Ni_{20}Co_{20}Al_{20}$ form a Cr_2O_3/SiO_2 layer and an Al_2O_3 layer, respectively.[44] The Cr_2O_3/SiO_2 layer leads to a lower oxidation resistance for $Fe_{20}Cr_{20}Ni_{20}Co_{20}Si_{20}$. Excessive Si addition shows negative effects on oxidation resistance, leading to the formation of intermetallic compounds that can act as diffusion channels for oxygen, resulting in internal oxidation.[80] Moreover, the effect of Ti on the properties of FeCrNiCoAl alloys has been studied.[81,82] When Al is partially substituted by Ti, the increased Ti content in the FeCrNiCoAlTi system promotes the formation of the FCC phase and leads to good mechanical properties.[83] The Ti addition also enhances oxidation resistance due to its higher oxide-forming ability, diminishing the external oxidation of Cr and promoting the formation of an external oxide layer composed of Ti and Fe oxides.[81] However, excessive Ti addition leads to a discontinuous Cr_2O_3 layer and a lower oxidation resistance.[84,85] Therefore, the addition of Ti should be limited to small amounts to adjust the microstructure and mechanical properties.

According to the phase diagram calculation shown in Appendix Table 4 and Appendix Fig. 18, the FeCrNiCoCuAl system exhibits a low melting point, and phase structure predictions indicate the presence of a liquid phase at 1000 °C. In contrast, the FeCrNiCoAl system with varying Al content shows no liquid phase at 1000 °C (Appendix Fig. 19), however, the sigma phase occurs in FeCrNiCoAl systems below 1000 °C. For example, the volume fraction of the sigma phase is around 30% at 700–900 °C but is 0% at temperatures above 1000 °C. Overall, it is suggested that the FeCrNiCoAl system can perfectly replace the FeCrNiCoCuAl system for HT applications above 1000 °C.

3. Other transition metal ternary systems and sub-systems

By reducing the number of elements, MEAs containing around three primary elements may offer cost benefits along with performance benefits. A series of MEAs is listed in Appendix Table 5. Fig. 10 presents the mass gain curves of several ternary alloys, including those of FeCoNi, FeCrNi, and CoCrNi, after oxidation at various temperatures. Among these, FeCrNi exhibits the lowest and most stable mass gain, ranging from 0.28 mg cm^{-2} at 800 °C to 0.91 mg cm^{-2} at 1000 °C after 100 hours.[86] In contrast, FeCoNi shows the highest mass gain, from 5.2 mg cm^{-2} at 800 °C to 19.8 mg cm^{-2} at 1000 °C after only 28 hours.[87] CoCrNi has a mass gain of 2 mg cm^{-2} at 900 °C to 2.5 mg cm^{-2} at 1000 °C after 48 hours.[88] The significant difference in k_w values between FeCoNi and FeCrNi, 12.96 mg^2 cm^{-4} h^{-1} and 7.2×10^{-3} mg^2 cm^{-4} h^{-1}, respectively, at 1000 °C, indicates that FeCrNi forms a protective oxidation layer that resists the penetration and diffusion of oxygen.

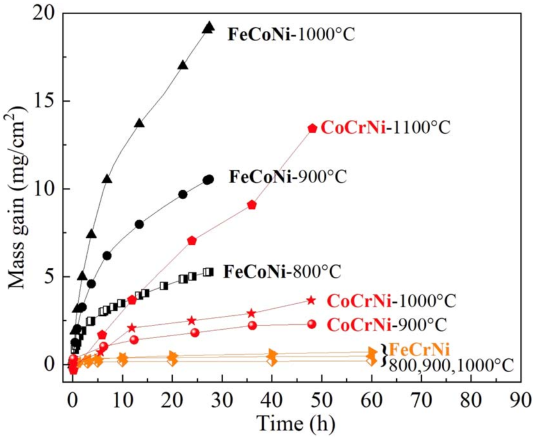

Fig. 10 Oxidation mass gain curves of ternary MEAs, including FeCoNi,[60] FeCrNi,[86] and CoCrNi.[41]

Comparing the above oxidation data, the presence of Cr in FeCrNi significantly contributes to its oxidation resistance. At temperatures ranging from 800–1000 °C, Cr_2O_3 acts as the main protective layer for FeCrNi after 100 hours of oxidation.[86] This stable Cr_2O_3 layer effectively reduces mass gain and enhances the overall oxidation resistance of the alloy. Although CoCrNi includes Cr, it forms a thin inner layer of Cr_2O_3 and a main layer of $CoCr_2O_4$.[88] After 48 hours, the oxide layer for CoCrNi becomes unstable, and the adhesion between different oxide layers weakens, compromising its overall oxidation resistance. For FeCoNi, the formation of $CoNiO_2$ and Fe oxides on the surface leads to high mass gain,[60] which indicates less effective protection against oxidation.

Adding Al or a combination of Al and Mo to the FeCoNi system has been proven as an effective strategy for enhancing oxidation resistance.[87,89] For instance, by adding 5–20 at% of Al, the mass gain of FeCoNi (35.5 mg cm^{-2}) is reduced to 28.6–20.9 mg cm^{-2}. The incorporation of Al leads to the formation of a protective Al_2O_3 layer, significantly reducing mass gain and improving the alloy's HT performance. In summary, the presence of Cr and Al in ternary alloys such as FeCrNi and FeCoNi plays a crucial role in forming protective oxide layers that enhance oxidation resistance. The performance of these alloys at high temperatures is heavily influenced by the type and stability of the oxide layers formed. Further exploration of element additions, such as Si and Mo, may provide additional

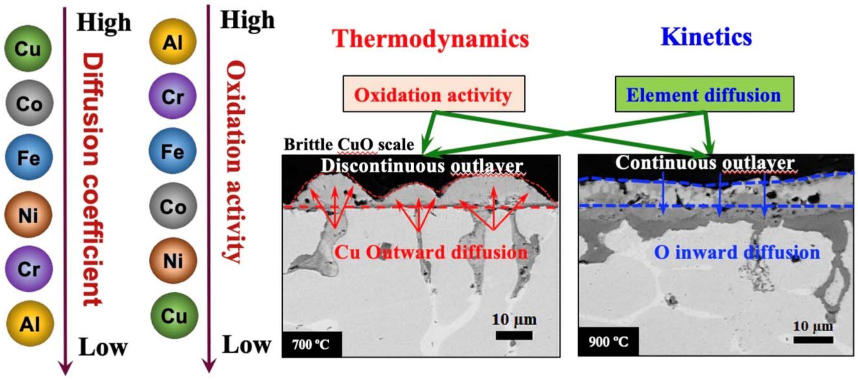

Fig. 11 Interplay of thermodynamics and kinetics in the FeCrNiCoAlCu system[66] (reproduced from ref. 66 with permission from [Elsevier], copyright [2022]).

improvements in oxidation resistance and overall mechanical properties.

4. General discussion and perspective

4.1. Understanding protection and failure mechanisms

Alloys designed for HT oxidizing conditions rely heavily on forming exterior oxide scales, which imparts resistance to hot corrosion and oxidation.[53,90] For the oxide scale to be beneficial, it must be thermodynamically, chemically and mechanically stable.[28] Both thermodynamic and kinetic factors influence the oxidation resistance and failure mechanisms of the oxide scale. As illustrated in Fig. 11, the investigation into the Fe–Co–Cr–Ni–Cu–Al system has shown that the interplay of these two factors primarily governs TGO formation. As shown in Fig. 11, Cu with the highest diffusion coefficient, predominantly diffuses outward, forming a discontinuous oxide layer on the surface.[66] In contrast, Cr shows slow diffusivity and exhibits a relatively high oxidation activity compared to the other TMs, and thus ends up as a slow-growing Cr-rich protective oxide scale for steels and alloys in various HT corrosive environments. In addition, Al has a high oxidation activity and is preferentially oxidized to form a protective pure or Al_2O_3-rich scale on the alloy surface. Therefore, the HT oxidation rate of the TM HEAs is significantly reduced with the addition of Al.

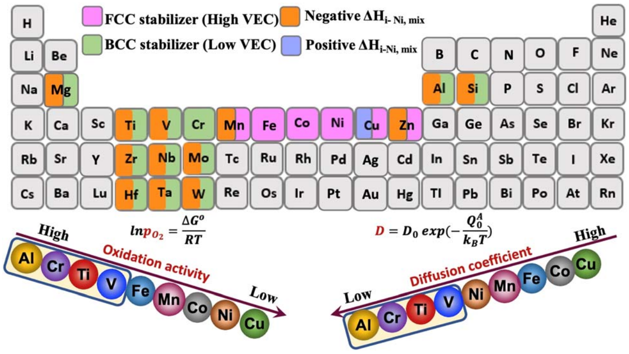

Fig. 12 Periodic table for the selection of CCA elements, showing oxidation activity (reflected by p_{O_2}) and diffusion coefficient (D) data from ref. 66, mixing enthalpy of binary pairs ($\Delta H_{i\text{–Ni,mix}}$) data from ref. 93, and VEC values from ref. 92. Note that the binary pairing-enthalpy of element *i* with Ni is used as the benchmark, aligning with Ni-based HT alloys.

To design effective TM-CCAs, it is crucial to selectively incorporate elements that act as FCC/BCC stabilizers to obtain good mechanical properties and tailor diffusion rates. These elements should possess negative enthalpy, associated with the priority of dissolving in the matrix phase instead of segregating in a low-entropy phase as a fast diffusion channel, as well as exhibit high oxidation activity and a low diffusion rate to build a high-quality oxide scale at elevated temperatures.[91] This strategic incorporation can be guided by data such as valence electron concentration (VEC) values,[92] binary pair enthalpy of mixing ($\Delta H_{i-j,\text{mix}}$),[93] the equilibrium partial pressure of oxygen (p_{O_2}),[68] and diffusion coefficients (D),[66] as shown in Fig. 12. The $\ln p_{O_2}$ and D can be calculated through the following equations separately.

$$\ln p_{O_2} = \frac{2\Delta G^\circ}{RT} \tag{1}$$

where ΔG° is the standard free energy change, R is the ideal gas constant, and T is temperature.

$$D = D_0 \exp\left(-\frac{Q_0^A}{k_B T}\right) \tag{2}$$

where D_0 is the pre-exponential factor, Q_0^A is the activation energy, and k_B is the Boltzmann's constant.

This strategy developed a novel class of CCA, $AlTiVCrNi_5$, by selecting components with low VEC, highly negative $\Delta H_{i-j,\text{mix}}$ with Ni, low diffusion rate, and high oxidation activity.[91] After oxidation at 1000 °C, a complex concentrated oxide (CCO) is developed. It is found that this CCO shows unique thermos-mechanical properties, including high thermodynamic stability, low thermal expansion, high fracture tolerance, and an excellent combination of strength and ductility. This study shows great promising potential to offer a fresh perspective on designing and developing advanced materials that boast exceptional functionality and versatility.

4.2. Improving design and experimental methods

One of the major challenges in CCA research is the inefficiency of design and preparation methods. Traditional experimental approaches are time-consuming and resource-intensive. To overcome this, high-throughput techniques are being increasingly adopted.[94,95] These techniques enable rapid screening of a large number of alloy compositions, significantly accelerating the discovery and optimization process. A combined approach utilizing phase diagram calculations (CALPHAD), DFT, and oxidation resistance assessments to systematically design and evaluate new alloys should be used. This approach will provide a comprehensive understanding of the alloys' behavior under HT conditions, allowing for more efficient and targeted alloy development. CALPHAD is instrumental in designing alloys with desired phase structures, such as FCC + BCC, while avoiding intermetallics such as Laves and Sigma phases. For instance, Appendix Fig. 14–22 present the stable phase diagrams of all the commonly used CCAs discussed in this paper. Additionally, DFT calculations assist in determining the diffusivity of each element within each various phase, aiding in the prediction of oxidation layer formation.

Comparative studies have shown that CCAs exhibit similar or lower oxidation/corrosion resistance than Fe- and Ni-based traditional HT alloys (such as 310S and Inconel 625) below 800 °C, while displaying higher resistance above 900 °C.[44,96–98] Therefore, it is essential to ensure that the operational temperature of CCAs for future applications remains above 800 or 900 °C to fully exploit their superior oxidation resistance. Additionally, a schematic diagram illustrating the mass gain curves over time, highlighting the transition from the initial rapid oxidation stage to the stable steady-state stage, can provide valuable insights into the long-term performance of these alloys and can extend the test time to above 48 hours.

4.3. Developing standards and towards artificial intelligence

The current review aims to promote data sharing in the field of oxidation of CCAs. Fig. 13 presents a co-citation network of publications from the period of 2004–2024 and their citation relations using the Web of Science search engine.[99] The search employed the queries of 'CCAs (or HEAs/MEAs)' and 'Corrosion/Oxidation' in all types of documents under the 'Topic' search. The resulting cluster highlights extensive research conducted on the corrosion and oxidation of CCAs. However, the complexity of the alloy's chemical composition makes it difficult for researchers to compare and establish predictive long-term corrosion kinetic models.

Machine learning (ML) offers transformative potential in materials science, particularly in the intelligent design of HT CCAs.[100,101] By leveraging vast datasets and advanced algorithms, ML can accelerate the identification of promising alloy compositions through complex pattern recognition and predict alloy performance with high accuracy. A study on phase prediction of CCAs exemplifies this, using an experimental dataset of 401 different HEA compositions and phases to train three ML algorithms: K-nearest neighbours (KNN), support vector machine (SVM), and artificial neural network (ANN).[102] For scenarios classifying three phases using parameters such as VEC, ΔH_{mix} (mixing enthalpy), ΔS_{mix} (mixing entropy), δ (atomic radius difference), and $\Delta\chi$ (electronegativity difference), the accuracy rates for KNN, SVM and ANN models have been reported as 68.6%, 64.3% and 74.3%, respectively. Although these ML methods have achieved reasonable accuracy, there is still room for improvement. While VEC, ΔH_{mix}, ΔS_{mix}, δ, and $\Delta\chi$ are the most commonly used parameters in HEA phase prediction, additional parameters, such as atomic polarizability, should be

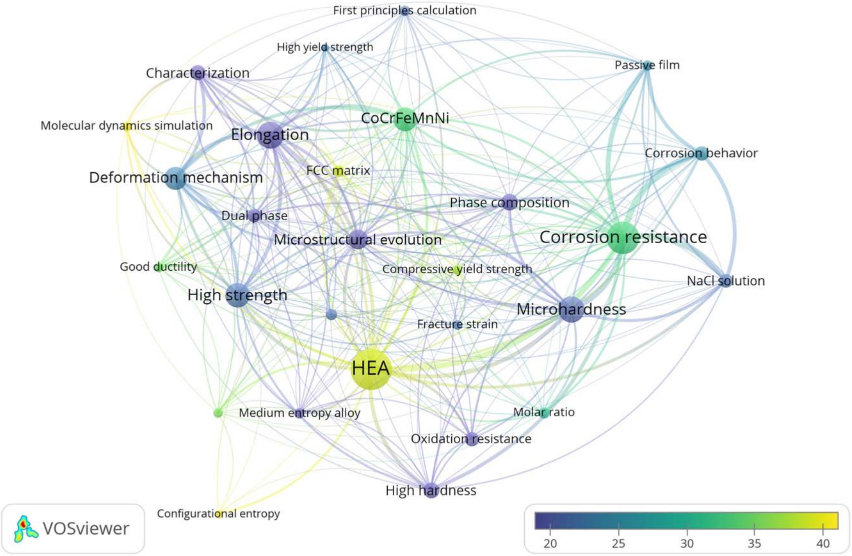

Fig. 13 Visualization of the co-citation network of 'CCAs (or HEAs/MEAs)' and 'Corrosion/Oxidation' publications. Citation relations from 2004 to 2024 (VOSviewer[99]).

considered for performance improvements.[103–105] Identification and use of the most influential parameters as input features for CCA phase prediction models can enhance model accuracy. However, it is challenging to conclude which physical parameters have the highest correlation due to variations in datasets and ML algorithms.[103] To address this issue, it is suggested to build a public dataset using CALPHAD as a first step to minimize dataset discrepancies. The integration of CALPHAD with artificial intelligence (AI) techniques presents a major opportunity for optimizing alloy design, enabling the efficient exploration of the compositional space and the identification of optimal properties. Furthermore, developing standardized testing protocols and performance benchmarks for CCAs is essential. These standards will ensure consistency and reliability in experimental data, facilitating the comparison of results across different studies and accelerating the overall progress in this field.

Understanding the protection and failure mechanisms of corrosion product layers, improving design and experimental methods, and leveraging ML and advanced computational techniques will aid in the future development of high-performance CCAs. Addressing these aspects can significantly enhance the oxidation resistance and overall performance of CCAs for HT applications, broadening their applicability across various industries.

5. Conclusions

HT applications are essential for industries seeking enhanced performance of engine components. CCAs represent the forefront of high-performance alloys in this context. Therefore, understanding the protection and failure mechanisms of corrosion product layers, improving design and experimental methods, and leveraging ML and advanced computational techniques are crucial for the future development of high-performance CCAs. This work reviews the oxidation resistance and overall performance of CCAs in HT applications and challenges in the field. The following key aspects are summarized.

(1) Cantor alloy systems exhibit good oxidation resistance primarily due to the formation of stable protective oxide layers, such as Cr_2O_3. Elemental additions, notably Al, further enhance this resistance by promoting the formation of Al_2O_3 layers, which serve as robust barriers against oxidation. Conversely, elements such as Cu and Mn can compromise the integrity of the protective oxide layer, thereby reducing the overall oxidation resistance.

(2) MEA systems, particularly FeCrNi, demonstrate excellent oxidation resistance due to the formation of stable Cr_2O_3 layers. In contrast, systems such as FeCoNi demonstrate higher mass gains and less stable oxide layers in the absence of Cr, highlighting the need for further optimization to enhance their oxidation resistance.

(3) A deep understanding of the thermodynamic and kinetic factors that influence oxide scale stability is essential for improving the alloy's HT performance. Selective incorporation of elements based on these principles can significantly enhance the properties of CCAs. Balancing the factors such as oxidation activity, diffusion coefficients, VEC values, and binary pair enthalpy of mixing is crucial to achieving the desired HT properties.

(4) The advancement of CCAs relies heavily on innovative design and experimental methods. High-throughput techniques enable rapid screening and optimization of alloy compositions. Computational approaches, including CALPHAD and DFT, play a pivotal role in predicting phase stability and oxidation behavior, providing valuable insights into the properties of potential alloy compositions before experimental validation.

(5) ML offers promising avenues for the intelligent design and prediction of alloy performance. By analyzing vast datasets, ML can identify patterns and predict the behavior of new alloy compositions under diverse conditions. When combined with traditional computational techniques, ML can significantly enhance the efficiency and accuracy of alloy development, leading to the discovery of novel CCAs with superior properties.

Data availability

No primary research results, software or code have been included, and no new data were generated or analysed as part of this review.

Author contributions

Haofei Sun: investigation, data curation, formal analysis, writing – original draft, writing – review and editing. Emily Seto: data curation, validation, writing – review and editing. Meifeng Li: supervision, methodology, writing – review and editing. jing liu: supervision, funding acquisition, conceptualization, resources, writing – review and editing.

Conflicts of interest

There are no conflicts to declare.

Appendices

Appendix A: oxidation data

Table 1 Oxidation data of the FeCrNiCoMn system

Ref.	T/°C	Time/h	Materials (mol%)	Weight gain (mg cm^{-2})	parabolic rate constant k_w (mg^2 cm^{-4} h^{-1})	Activation energy (kJ mol^{-1})	Predicted phases (vol%)
LaPlanche, *et al.* 2016 (ref. 43)	600	100	$Fe_{20}Cr_{20}Ni_{20}Co_{20}Mn_{20}$	0.3	0.015	130	69% FCC_L12, 31% sigma
	700			1	0.020		81% FCC_L12, 19% sigma
	800			2.2	0.060		96% FCC_L12, 4% sigma
	900	88		3	0.149		FCC_L12
Kai, *et al.* 2017 (ref. 44)	700	48	$Fe_{20}Cr_{20}Ni_{20}Co_{20}Mn_{20}$	1	0.018	109 (700–850 °C)	81% FCC_L12, 19% sigma
	800			2.1	0.054		96% FCC_L12, 4% sigma
	850			—	0.079		FCC_L12
	900			3.2	0.104		FCC_L12
Kim *et al.*, 2018 (ref. 47)	900	24	$Fe_{20}Cr_{20}Ni_{20}Co_{20}Mn_{20}$	1.76	0.13	—	FCC_L12
	1000			4.45	0.83		FCC_L12
	1100			9.08	3.44		FCC_L12
Adomako, *et al.*, 2018 (ref. 41)	800	24	$Fe_{20}Cr_{20}Ni_{20}Co_{20}Mn_{20}$	0.7	3.41×10^{-4}	203	96% FCC_L12, 4% sigma
	850			0.85	5.60×10^{-4}		FCC_L12
	900			1.35	1.27×10^{-3}		FCC_L12
	1000			4.0	0.012		FCC_L12
Huang, *et al.*, 2019 (ref. 42)	700	100	$Fe_{20}Cr_{20}Ni_{20}Co_{20}Mn_{20}$	1.07	2.4×10^{-4}	—	81% FCC_L12, 19% sigma
	800			2.1	7.5×10^{-4}		96% FCC_L12, 4% sigma
	900			2.95	1.35×10^{-3}		FCC_L12
Ye, *et al.*, 2020 (ref. 48)	900	100	$Fe_{20}Cr_{20}Ni_{20}Co_{20}Mn_{20}$	1.64	1.302×10^{-4} (0–10 h), 4.259×10^{-5} (10–100 h)	—	FCC_L12
Cui, *et al.*, 2020 (ref. 49)	600	100	$Fe_{20}Cr_{20}Ni_{20}Co_{20}Mn_{20}$	0.30	1.19×10^{-5}	—	69% FCC_L12, 31% sigma
Agustianingrum, *et al.*, 2020 (ref. 45)	900	48	$Fe_{20}Cr_{20}Ni_{20}Co_{20}Mn_{20}$	2.5	0.18	255.1	FCC_L12
	1000			7.5	1.347		FCC_L12
	1100			19.7	8.167		FCC_L12
	900	48	$Fe_{39}Cr_{18}Ni_{14}Co_{16}Mn_{13}$	2.6	0.291	233.9	FCC_L12
	1000			10.0	2.030		FCC_L12
	1100			22.0	9.563		FCC_L12
	900	48	$Fe_{59}Cr_{11}Ni_{10}Co_{10}Mn_{10}$	21.0	9.693	116.2	FCC_L12
	1000			30.0	21.13		FCC_L12
	1100			51.0	55.46		FCC_L12

Table 2 Oxidation data of the FeCrNiCoMn + M system

Ref.	*T*/°C	Time/h	Materials (mol%)	Weight gain (mg cm^{-2})	parabolic rate constant k_w (mg^2 cm^{-4} h^{-1})	Predicted phases (vol%)
Cui, *et al.*, 2020 (ref. 49)	600	100	$Fe_{19}Cr_{19}Ni_{19}Co_{19}Mn_{19}Al_5$	0.254	1.06×10^{-5}	30% BCC_B2, 32% FCC_L12, 38% sigma
			$Fe_{18}Cr_{18}Ni_{18}Co_{18}Mn_{18}Al_9$	0.224	1.05×10^{-5}	56% BCC_B2, 44% sigma
			$Fe_{17}Cr_{17}Ni_{17}Co_{17}Mn_{17}Al_{13}$	0.190	7.8×10^{-6}	58% BCC_B2, 42% sigma
Ye, *et al.*, 2020 (ref. 48)	900	100	$Fe_{18}Cr_{18}Ni_{18}Co_{18}Mn_{18}Al_{10}$	1.51	1.234×10^{-4} (0–10 h) 3.334×10^{-6} (10–100 h)	40% BCC_B2, 22% sigma, 38% FCC_L12
			$Fe_{17}Cr_{17}Ni_{17}Co_{17}Mn_{17}Al_{17}$	1.32	1.199×10^{-4} (0–10 h) 2.037×10^{-6} (10–100 h)	61% BCC_B2, 39% sigma
			$Fe_{15}Cr_{15}Ni_{15}Co_{15}Mn_{15}Al_{23}$ (FCC + BCC)	1.23	8.664×10^{-5} (0–10 h) 2.037×10^{-6} (10–100 h)	68% BCC_B2, 32% BCC_B2#2
			$Fe_{14}Cr_{14}Ni_{14}Co_{14}Mn_{14}Al_{29}$ (FCC + BCC)	1.08	4.667×10^{-5} (0–10 h) 1.667×10^{-6} (10–100 h)	73% BCC_B2, 27% BCC_B2#2
Moghaddam, *et al.*, 2021 (ref. 59)	700	10	$Fe_{20}Cr_{20}Ni_{19}Co_{19}Mn_{19}Al_5$	0.30		20% BCC_B2, 52% FCC_L12, 28% sigma
	900			0.77		89% FCC_L12, 11% BCC_B2
Huang, *et al.*, 2019 (ref. 42)	700	100	$Fe_{19}Cr_{19}Ni_{19}Co_{19}Mn_{19}Nb_5$	0.32	2×10^{-5}	14% C14_Laves, 34% MNNI_L10, 3% N13TA_D0A, 49% sigma
	800			1.24	2.4×10^{-4}	17% C14_Laves, 37% MNNI_L10, 46% sigma
	900			3.17	1.65×10^{-3}	13% C14_Laves, 87% FCC_L12

Table 3 Oxidation data of the FeCrNiCo system

Ref.	T/°C	Time/h	Materials (mol%)	Weight gain (mg cm^{-2})	parabolic rate constant k_w (mg^2 cm^{-4} h^{-1})	Predicted phases (vol%)
Kai, *et al.*, 2004 (ref. 60)	800	72	$Fe_{25}Cr_{25}Ni_{25}Co_{25}$	0.23	7.02×10^{-4}	FCC_L12
	850			1.15	(1) 0.00144 (2) 0.23	FCC_L12
	900			1.62	(1) 0.00637 (2) 0.11 (3) 0.0249	FCC_L12
	950			1.83	(1) 0.0133 (2) 0.0824 (3) 0.0204	FCC_L12
	1000			2.25	(1) 0.0147 (2) 0.355 (3) 0.0612	FCC_L12
Kai, *et al.*, 2020 (ref. 61)	700	48	$Fe_{20}Cr_{20}Ni_{40}Co_{20}$	0.14	1.21×10^{-4}	FCC_L12
	800			0.3	1.36×10^{-2} (0–2.8 h) 9.4×10^{-4} (4.3–48 h)	FCC_L12
	900			0.9	1.29×10^{-3} (0–2.3 h) 1.2 (2.8–4 h) 2.82×10^{-3} (5.4–48 h)	FCC_L12
Dąbrowa, *et al.*, 2021 (ref. 62)	1000	500	$Fe_{27}Cr_{26}Ni_{21}Co_{26}$	6.4	—	FCC_L12

Table 4 Oxidation data of the FeCrNiCo + M system

Ref.	T/°C	Time/h	Materials (mol%)	Weight gain (mg cm^{-2})	parabolic rate constant k_w (mg^2 cm^{-4} h^{-1})	Predicted phases (vol%)
Kai, *et al.*, 2004 (ref. 60)	800	28	$Fe_{20}Cr_{18}Ni_{22}Co_{21}Cu_{19}$	0.50	0.0068	20% FCC_L12, 80% FCC_L12#2
	850			1.00	0.0168	20% FCC_L12, 80% FCC_L12#2
	900			1.24	0.0232	20% FCC_L12, 80% FCC_L12#2
	950			3.18	0.252	20% FCC_L12, 80% FCC_L12#2
	1000			6.11	1.38	20% FCC_L12, 80% FCC_L12#2
Butler, *et al.*, 2015 (ref. 74)	1050	100	$Fe_{22}Cr_{22}Ni_{23}Co_{23}Al_{10}$	1.8	0.047	22% BCC_B2#2, 88% FCC_L12
Butler, *et al.* 2016 (ref. 73)	1050	100	$Fe_{23}Cr_{24}Ni_{22}Co_{23}Al_8$	1.8	0.09 (1–30 h) 0.009 (30–100 h)	87% FCC_L12, 13% BCC_B2
			$Fe_{22}Cr_{23}Ni_{24}Co_{22}Al_{10}$	1.6	0.086 (1–19 h) 0.0065 (19–100 h)	78% FCC_L12, 22% BCC_B2#2
			$Fe_{22}Cr_{22}Ni_{23}Co_{22}Al_{12}$	1.5	0.0068 (1–19 h) 0.0017 (19–100 h)	68% FCC_L12, 32% BCC_B2#2
			$Fe_{21}Cr_{22}Ni_{21}Co_{21}Al_{16}$	1.1	0.17 (2–18 h) 0.015 (19–36 h)	46% FCC_L12, 52% BCC_B2#2, 2% BCC_B2
			$Fe_{20}Cr_{21}Ni_{19}Co_{20}Al_{20}$	0.9	0.29 (2–18 h) 0.0058 (12–50 h)	69% BCC_B2#2, 31% BCC_B2
			$Fe_{18}Cr_{18}Ni_{17}Co_{18}Al_{29}$	0.4	0.0068 (2 h–10 h)	77% BCC_B2#2, 23% BCC_B2
Kai *et al.*, 2017 (ref. 44)	700	48	$Fe_{21}Cr_{20}Ni_{20}$ $Co_{19}Al_{20}$	0.046	0.000306 (0–3 h) 9.36×10^{-6} (3–48 h)	69% BCC_B2#2, 31% sigma
	800			0.085	0.000144	69% BCC_B2#2, 31% sigma
	900			0.28	0.001764	71% BCC_B2#2, 29% sigma
	700		$Fe_{20}Cr_{20}Ni_{20}$ $Co_{20}Si_{20}$	0.10	0.000151	41% BCC_B2#2, 27% Cr3Si_A15, 32% Ni5Si2
	800			0.15	0.000648	25% Cr3Si_A15, 11% Ni5Si2, 47% FCC_L12#2, 17% Co2Si1
	900			0.44	0.00396	21% Cr3Si_A15, 53% FCC_L12#2, 26% Co2Si1
Dąbrowa, 2017 (ref. 65)	1000	100	$Fe_{20}Cr_{20}Ni_{20}$ $Co_{20}Al_{20}$	0.98	0.0034	71% BCC_B2#2, 29% BCC_B2
			$Fe_{18}Cr_{18}Ni_{18}$ $Co_{18}Al_{18}Cu_9$	0.56	0.0012	55% BCC_B2#2, 3% FCC_L12#2, 37% BCC_B2#3, 5% liquid
			$Fe_{17}Cr_{17}Ni_{17}Co_{17}Al_{17}Cu_{17}$	0.21	0.00029	46% BCC_B2#2, 6% FCC_L12#2, 32% BCC_B2, 16% liquid
Liu, *et al.*, 2019 (ref. 72)	1000	100	$Fe_{21}Cr_{21}Ni_{20}Co_{19}Cu_{19}$	1.3	1.94×10^{-4} (0–9 h) 1.37×10^{-4} (9–100 h)	20% FCC_L12, 80% FCC_L12#2
			$Fe_{19}Cr_{20}Ni_{19}Co_{18}Cu_{16}Al_8$	0.72	5.86×10^{-5} (0–16 h) 4.27×10^{-5} (16–100 h)	68% FCC_L12#2, 6% BCC_B2, 26% liquid
			$Fe_{17}Cr_{18}Ni_{14}Co_{19}Cu_{17}Al_{16}$	0.33	8.76×10^{-6}	40% BCC_B2#2, 5% FCC_L12#2, 34% BCC_B2, 21% liquid
			$Fe_{17}Cr_{17}Ni_{16}Co_{14}Cu_{13}Al_{23}$	0.26	5.50×10^{-6}	31% BCC_B2#3, 61% BCC_B2, 8% liquid
			$Fe_{15}Cr_{15}Ni_{16}Co_{13}Cu_{13}Al_{28}$	0.25	4.64×10^{-6}	73% BCC_B2#2, 24% BCC_B2#3, 2% liquid

Table 4 (*Contd.*)

Ref.	T/°C	Time/h	Materials (mol%)	Weight gain (mg cm^{-2})	parabolic rate constant k_w (mg^2 cm^{-4} h^{-1})	Predicted phases (vol%)
Abbaszadeh, *et al.*, 2020 (ref. 106)	800	72	$Fe_{18}Cr_{18}Ni_{18}Co_{18}Cu_{18}Al_9$ (FCC + BCC)	0.33	0.0011	31% BCC_B2#2, 19% FCC_L12, 34% FCC_L12#2, 16% sigma
	900			0.42	0.0032	26% BCC_B2#2, 20% FCC_L12, 49% FCC_L12#2, 6% sigma
	1000			0.95	0.014	59% FCC_L12#2, 12% BCC_B2, 28% liquid
Huang, *et al.*, 2021 (ref. 76)	1000	2	$Fe_{19}Cr_{19}Ni_{19}Co_{19}Cu_{23}$	10	0.516	26% FCC_L12, 74% FCC_L12#2
	1050			10	0.468	26% FCC_L12, 74% FCC_L12#2
	1100			26	4.89	26% FCC_L12, 74% FCC_L12#2
	1130			58	9.9	75% FCC_L12#2, 25% liquid
	1250			172	258	73% FCC_L12#2, 27% liquid
	1340			175	443.4 (0–1.5 h) 25.74 (1.5–2 h)	Liquid
Li, *et al.*, 2022 (ref. 66)	700	100	$Fe_{20}Cr_{20}Ni_{20}Co_{20}Cu_{20}$	2.5		21% FCC_L12, 79% FCC_L12#2
	800			2.9		21% FCC_L12, 79% FCC_L12#2
	900			3.3		21% FCC_L12, 79% FCC_L12#2
	700		$Fe_{20}Cr_{20}Ni_{20}Co_{20}Cu_{15}Al_5$	1.2		14% BCC_B2#2, 16% FCC_L12, 60% FCC_L12#2, 9% sigma
	800			1.9		10% BCC_B2#2, 18% FCC_L12, 72% FCC_L12#2
	900			2.6		19% FCC_L12, 75% FCC_L12#2, 6% BCC_B2
	700		$Fe_{20}Cr_{20}Ni_{20}Co_{20}Cu_{10}Al_{10}$	0.4		37% BCC_B2#2, 9% FCC_L12, 33% FCC_L12#2, 22% sigma
	800			1.7		9% FCC_L12, 46% FCC_L12#2, 14% sigma, 32% BCC_B2
	900			1.8		9% FCC_L12, 61% FCC_L12#2, 3% sigma, 28% BCC_B2
Mohanty, *et al.*, 2019 (ref. 28)	1100	200	$Fe_{23}Cr_{23}Ni_{23}Co_{23}Al_7$	1.10	1.02×10^{-4}	91% FCC_L12, 9% BCC_B2
			$Fe_{22}Cr_{22}Ni_{22}Co_{22}Al_{14}$ (FCC + BCC)	0.44	2.28×10^{-5}	70% FCC_L12, 30%, BCC_B2#2
Gawel *et al.*, 2021 (ref. 107)	1000	48	$Fe_{15}Cr_{25}Ni_{20}Co_{35}Al_4$	2.1	0.07344 (1–13 h) 0.1044 (13–32 h) 0.08028 (32–48 h)	99% FCC_L12, 1% BCC_B2
			$Fe_{15}Cr_{21}Ni_{35}Co_{24}Al_5$	4.1	0.05004 (1–13 h), 0.09036 (13–32 h) 0.06156 (32–48 h)	FCC_L12
Kai, *et al.*, 2020 (ref. 61)	700	48	$Fe_{17}Cr_{16}Ni_{34}Co_{16}Al_{17}$	0.04	4.25×10^{-5}	66% BCC_B2#2, 27% FCC_L12, 7% sigma
	800			0.12	2.87×10^{-4}	61% BCC_B2#2, 39% FCC_L12
	900			0.28	1.41×10^{-3} (0–8.5 h) 5.9×10^{-4} (11.1–48 h)	57% BCC_B2#2, 43% FCC_L12
	700	48	$Fe_{18}Cr_{18}Ni_{36}Co_{18}Al_9$	0.09	6.34×10^{-5}	34% BCC_B2#2, 66% FCC_L12
	800			0.15	4.21×10^{-4}	28% BCC_B2#2, 72% FCC_L12
	900			0.38	4.32×10^{-3} (0–11 h) 1.9×10^{-3} (12–48 h)	22% BCC_B2#2, 78% FCC_L12
Zhu, *et al.*, 2020 (ref. 77)	800	100	$Fe_{26}Cr_{22}Ni_{25}Co_{25}Al_1$ (BCC)	0.99	—	FCC_L12
	900			1.49	—	FCC_L12
	1000			2.53	—	FCC_L12
Ham, *et al.*, 2021 (ref. 82)	1100	24	$Fe_{20}Cr_{20}Ni_{19}Co_{19}Al_{22}$ (BCC + FCC)	0.75	—	72% BCC_B2#2, 28% BCC_B2
			$Fe_{20}Cr_{20}Ni_{19}Co_{20}Al_{20}Ti_1$ (BCC + FCC)	0.17	—	—

Table 4 (*Contd.*)

Ref.	T/°C	Time/h	Materials (mol%)	Weight gain (mg cm^{-2})	parabolic rate constant k_w (mg^2 cm^{-4} h^{-1})	Predicted phases (vol%)
Dąbrowa, *et al.*, 2021 (ref. 62)	1000	500	$Fe_{24}Cr_{25}Ni_{24}Co_{25}Al_3$	20.1	—	FCC_L12
			$Fe_{23}Cr_{24}Ni_{22}Co_{24}Al_6$	18.4	—	94% FCC_L12, 6% BCC_B2
			$Fe_{23}Cr_{23}Ni_{22}Co_{23}Al_9$	19.4	—	21% BCC_B2#2, 79% FCC_L12
			$Fe_{22}Cr_{22}Ni_{22}Co_{22}Al_{12}$	8.3	—	35% BCC_B2#2, 65% FCC_L12
Garip, *et al.*, 2021 (ref. 108)	800	120	$Fe_{23}Cr_{21}Ni_{24}Co_{24}Al_8$	4.1	0.1399	27% BCC_B2#2, 73% FCC_L12
	875			4.7	0.1957	23% BCC_B2#2, 77% FCC_L12
	950			6.0	0.3105	82% FCC_L12#2, 18% BCC
	800		$Fe_{23}Cr_{21}Ni_{24}Co_{24}Al_9$	1.9	0.02954	32% BCC_B2#2, 68% FCC_L12
	875			3.8	0.1241	28% BCC_B2#2, 72% FCC_L12
	950			5.2	0.2289	24% BCC_B2#2, 76% FCC_L12
	800		$Fe_{22}Cr_{21}Ni_{23}Co_{23}Al_{11}$	1.5	0.01985	41% BCC_B2#2, 54% FC_L12, 5% sigma
	875			2.4	0.05112	37% BCC_B2#2, 63% FCC_L12
	950			3.6	0.1037	33% BCC_B2#2, 67% FCC_L12
Kumar, *et al.*, 2022 (ref. 109)	1050	55 h	$Fe_{16}Cr_{16}Ni_{35}Co_{17}Al_{16}$	−0.07	0.012	45% BCC_B2#2, 55% FCC_L12
			$Fe_{16}Cr_{14}Ni_{32}Co_{16}Al_{22}$	0.36	0.002	75% BCC_B2#2, 25% FCC_L12
			$Fe_{15}Cr_{24}Ni_{31}Co_{16}Al_{15}$	0.29	0.015	42% BCC_B2#2, 58% FCC_L12
			$Fe_{14}Cr_{21}Ni_{29}Co_{14}Al_{22}$	0.56	0.054	25% BCC_B2#2, 75% FCC_L12
Chen, *et al.*, 2018 (ref. 75)	800	100	$Fe_{22}Cr_{22}Ni_{22}Co_{22}Al_{13}$ (BCC + FCC)	0.17	1.26×10^{-4}	47% BCC_B2#2, 39% FCC_L12, 14% sigma
	900			0.61	0.00426	40% BCC_B2#2, 59% FCC_L12, 1% sigma
	1000			1.4	0.0206	35% BCC_B2#2, 65% FCC_L12
	800		$Fe_{20}Cr_{20}Ni_{20}Co_{20}Al_{12}Si_6$ (BCC)	0.2	1.94×10^{-4}	46% BCC_B2#2, 1% Cr2Ni2Si, 17% Cr3Si_A15, 37% FCC_L12
	900			0.62	0.00484	41% BCC_B2#2, 13% Cr3Si_A15, 46% FCC_L12
	1000			1.9	0.0218	37% BCC_B2#2, 9% Cr3Si_A15, 54% FCC_L12
Kai, *et al.*, 2018 (ref. 80)	700	48	$Fe_{23}Cr_{23}Ni_{24}Co_{23}Si_6$	0.12	3.95×10^{-6}	4% Cr2Ni2Si, 95% FCC_L12, 1% sigma
	800			0.2	1.16×10^{-5}	FCC_L12
	900			0.62	1.33×10^{-4}	FCC_L12
	700		$Fe_{23}Cr_{22}Ni_{22}Co_{22}Si_{11}$	0.08	2.79×10^{-6}	28% Cr2Ni2Si, 72% FCC_L12
	800			0.19	1.12×10^{-5}	21% Cr2Ni2Si, 79% FCC_L12
	900			0.49	1.08×10^{-4}	93% FCC_L12, 7% CrSi_A15
Lu, *et al.*, 2019 (ref. 110)	1100	1000	$Fe_{20}Cr_{20}Ni_{20}Co_{20}Al_{20}Y_{0.02}Hf_{0.02}$	—	0.000684	—
Moghaddam, *et al.*, 2021 (ref. 59)	700	10	$Fe_{20}Cr_{20}Ni_{21}Co_{21}Al_9Si_9$ (BCC + FCC)	0.28	—	4% BCC_B2, 41% BCC_B2#2, 28% Cr2Ni2Si, 2% Cr3Si_A15, 26% FCC_L12
	900			0.11	—	44% BCC_B2#2, 12% Cr3Si_A15, 45% FCC_L12
	1000			0.16	—	24% BCC_B2#2, 7% Cr3Si_A15, 69% FCC_L12
Li, *et al.*, 2021 (ref. 79)	1100	200	$Fe_{20}Cr_{20}Ni_{20}Co_{20}Al_{20}$	7.4	2.09 (stage 1) 0.1 (stage 2)	71% BCC_B2#2, 29% BCC_B2
			$Fe_{19}Cr_{19}Ni_{19}Co_{19}Al_{19}Si_4$	1.8	0.0137	36% BCC_B2, 64% BCC_B2#2
			$Fe_{18}Cr_{18}Ni_{18}Co_{18}Al_{18}Si_9$	6.6	1.8 (stage 1) 0.094 (stage 2)	21% BCC_B2, 64% BCC_B2#2, 15% Cr3Si_A15
			$Fe_{17}Cr_{17}Ni_{17}Co_{17}Al_{17}Si_{14}$	13.1	3.06 (stage 1) 0.313 (stage 2)	11% BCC_B2#2, 60% BCC_B2#3, 22% Cr3Si_A15
			$Fe_{16.5}Cr_{16.5}Ni_{16.5}Co_{16.5}Al_{16.5}Si_{16.5}$	15.5	4.176 (stage 1) 0.54 (stage 2)	15% BCC_B2#2, 57% BCC_B2#2, 8% Co2Si1, 21% Cr3Si_A15

Table 4 (*Contd.*)

Ref.	T/°C	Time/h	Materials (mol%)	Weight gain (mg cm^{-2})	parabolic rate constant k_w (mg^2 cm^{-4} h^{-1})	Predicted phases (vol%)
Liu, *et al.*, 2021 (ref. 81)	900	100	$Fe_{20}Cr_{20}Ni_{20}Co_{20}Al_{15}Ti_5$	0.60		—
			$Fe_{20}Cr_{17.5}Ni_{20}$ $Co_{20}Al_{15}Ti_{7.5}$	0.83		—
			$Fe_{20}Cr_{15}Ni_{20}Co_{20}Al_{15}Ti_{10}$	0.11		—
Yao-Jen, An-Chou, 2015 (ref. 84)	900	200	$Fe_{18}Cr_{18}Ni_{27}Co_{27}Ti_9$	5	—	—
			$Fe_{18}Cr_{18}Ni_{27}Co_{27}Ti_7Al_2$	3.2		—
			$Fe_{18}Cr_{18}Ni_{27}Co_{27}Ti_4Al_5$	2.4		—
			$Fe_{18}Cr_{18}Ni_{27}Co_{27}Ti_5Al_4$	1		—
Wang, *et al.*, 2019 (ref. 85)	700	100	$Fe_{20}Cr_{20}Ni_{20}Co_{20}Al_{10}Ti_{10}$ (BCC)	0.38	2.04×10^{-5} (1–20 h) 1.08×10^{-5} (20–100 h)	—
	900			1.65	3.66×10^{-4} (1–44 h) 1.18×10^{-4} (44–100 h)	—
	1100			2.85	4.2×10^{-3} (1–4 h) 5.4×10^{-4} (4–100 h)	—
	700		$Fe_{18}Cr_{18}Ni_{18}Co_{18}Al_{18}Ti_9$ (BCC)	0.22	7.2×10^{-6} (1–20 h) 1.75×10^{-6} (20–100 h)	—
	900			0.38	2.38×10^{-5} (1–44 h) 9.24×10^{-6} (44–100 h)	—
	1100			1.25	5.08×10^{-4} (1–4 h) 8.58×10^{-5} (4–100 h)	—
	700		$Fe_{17}Cr_{17}Ni_{17}Co_{17}Al_{25}Ti_8$ (BCC)	2.85	5.06×10^{-6} (1–20 h) 9.96×10^{-7} (20–100 h)	—
	900			0.22	1.97×10^{-5} (1–44 h) 9.12×10^{-6} (44–100 h)	—
	1100			0.38	3.47×10^{-4} (1–4 h) 6.18×10^{-5} (4–100 h)	—
Zhang, *et al.*, 2022 (ref. 111)	800	50	$Fe_{18}Cr_{18}Ni_{18}Co_{18}Al_{18}$ $(TiC)_8$	0.11	2.56×10^{-4}	—
	900			0.35	2.52×10^{-3}	—
	1000			0.79	1.38×10^{-2}	—
Liu, *et al.*, 2016 (ref. 112)	1050	100	$Fe_{24}Cr_{29}Ni_{21}Co_{22}Nb_2Si_2$	70	8.1×10^{-4}	5% C14_Laves, 95% FCC_L12
	1150			87	1.9×10^{-3}	3% C14_Laves, 97% FCC_L12
	1250			202	7.56×10^{-3}	85% FCC_L12, 15% liquid
	1050		$Fe_{23.5}Cr_{29}Ni_{21}Co_{22}Nb_2Si_2Mn_{0.5}$	63	7.2×10^{-4}	5% C14_Laves, 95% FCC_L12
	1150			81	1.62×10^{-3}	3% C14_Laves, 97% FCC_L12
	1250			190	6.45×10^{-3}	85% FCC_L12, 15% liquid
	1050		$Fe_{23}Cr_{29}Ni_{21}Co_{22}Nb_2Si_2$ Mn_1	61	6.72×10^{-4}	4% C14_Laves, 96% FCC_L12
	1150			77	1.45×10^{-3}	3% C14_Laves, 97% FCC_L12
	1250			183	5.41×10^{-3}	84% FCC_L12, 16% liquid
	1050		$Fe_{22}Cr_{29}Ni_{21}Co_{22}Nb_2Si_2$ Mn_2	60	5.76×10^{-4}	4% C14_Laves, 96% FCC_L12
	1150			73	1.33×10^{-3}	3% C14_Laves, 97% FCC_L12
	1250			177	4.78×10^{-3}	82% FCC_L12, 18% liquid
Chang, *et al.*, 2019 (ref. 113)	900	50	$Fe_{22}Cr_{11}Ni_{22}Co_{22}B_{22}$	8.9	—	37% FCC_L12, 63% M2B_C16
			$Fe_{20}Cr_{20}Co_{20}Ni_{20}B_{20}$	7.5	—	43% FCC_L12, 57% M2B_C16
			$Fe_{18}Cr_{27}Ni_{18}Co_{18}B_{18}$	6.5	—	49% FCC_L12, 51% M2B_C16
			$Fe_{17}Cr_{25}Ni_{17}Co_{17}B_{17}$	4.2	—	54% FCC_L12, 48% M2B_C16
			$Fe_{14}Cr_{43}Ni_{14}Co_{14}B_{14}$	3.1	—	59% Cr2B_CB, 31% FCC_L12

Table 5 Oxidation data of the MEA and MEA + M system

Ref.	T/°C	Time/h	Materials (mol%)	Weight gain (mg cm^{-2})	parabolic rate constant k_w (mg^2 cm^{-4} h^{-1})	Predicted phases (vol%)
Kai, *et al.*, 2004 (ref. 60)	800	28	$Fe_{31}Co_{34}Ni_{35}$	5.2	0.83	FCC_L12
	850			7.2	1.56	FCC_L12
	900			10.4	3.67	FCC_L12
	950			14.9	6.19	FCC_L12
	1000			19.8	12.96	FCC_L12
Xie, *et al.*, 2021 (ref. 87)	800	80	$Fe_{33}Co_{33}Ni_{33}$	35.5	0.0417	—
			$Fe_{32}Co_{32}Ni_{32}Al_5$	28.6	0.0345	—
			$Fe_{30}Co_{30}Ni_{30}Al_{10}$	27.5	0.0321	—
			$Fe_{28}Co_{28}Ni_{28}Al_{15}$	26.7	0.0321	—
			$Fe_{27}Co_{27}Ni_{27}Al_{20}$	20.9	0.025	—
Peng, *et al.*, 2023 (ref. 89)	800	100	$Fe_{20}Co_{20}Ni_{41}\ Al_{19}$	4.3	0.2034	60% BCC_B2#2, 15% FCC_L12#2, 25% FCC_L12
			$Fe_{19}Co_{19}Ni_{41}Al_{19}Mo_2$	1.3	0.0200	—
			$Fe_{18}Co_{18}Ni_{41}\ Al_{19}Mo_4$	1.9	0.0446	43% BCC_B2#2, 42% FCC_L12#2, 15% sigma
Sun, *et al.*, 2024 (ref. 86)	700	100	$Fe_{33}Cr_{33}Ni_{33}$	0.1	9.4×10^{-5}	14% BCC_B2, 86% FCC_L12
	800			0.28	5.3×10^{-4}	9% BCC_B2, 91% FCC_L12
	900			0.55	1.9×10^{-3}	3% BCC_B2, 97% FCC_L12
	1000			0.91	7.2×10^{-3}	FCC_L12
Zhang *et al.*, 2022 (ref. 114)	800	108	$Fe_{26}Cr_{21}Ni_{26}Mn_{27}$	1.72	0.0267	69% FCC_L12, 31% sigma
			$Fe_{25}Cr_{25}Ni_{25}Mn_{25}$	1.38	0.0167	60% FCC_L12, 40% sigma
			$Fe_{24}Cr_{28}Ni_{24}Mn_{25}$	1.45	0.0193	52% FCC_L12, 48% sigma
			$Fe_{23}Cr_{32}Ni_{22}Mn_{23}$	1.63	0.0247	42% FCC_L12, 58% sigma
Adomako, *et al.*, 2018 (ref. 41)	800	24	$Co_{33}Cr_{33}Ni_{33}$	0.03	2.43×10^{-7}	FCC_L12
	850			0.05	2.33×10^{-6}	FCC_L12
	900			0.075	1.51×10^{-5}	FCC_L12
	1000			0.65	2.87×10^{-4}	FCC_L12
	800		$Co_{25}Cr_{25}Ni_{25}Mn_{25}$	1.4	1.47×10^{-3}	83% FCC_L12, 17% sigma
	850			2.1	2.98×10^{-3}	91% FCC_L12, 9% sigma
	900			2.4	4.10×10^{-3}	99% FCC_L12, 1% sigma
	1000			5.7	0.0229	FCC_L12
Agustianingrum, *et al.*, 2020 (ref. 88)	900	48	$Co_{33}Cr_{33}Ni_{33}$	2	0.0439	FCC_L12
	1000			2.5	0.158	FCC_L12
	1100			12	2.94	FCC_L12
Butler, *et al.*, 2015 (ref. 74)	1050	500	$Al_{20}Co_{24}Cr_{25}Ni_{24}Si_6$	0.45	2.0×10^{-5}	6% BCC_B2, 58% BCC_B2#3, 3% Cr3Si_A15, 33% FCC_L12
			$Al_{15}Co_{35}Cr_{10}Ni_{35}Si_5$	0.1	4.8×10^{-5}	31% BCC_B2#2, 69% FCC_L12
Dąbrowa, 2017 (ref. 65)	1000	100	$Al_{29}Co_{29}Cr_{29}Cu_{14}$	0.56	0.0012	24% BCC_B2, 59% BCC_B2#4 18% FCC_l12

Appendix B: phase diagrams of common CCA systems

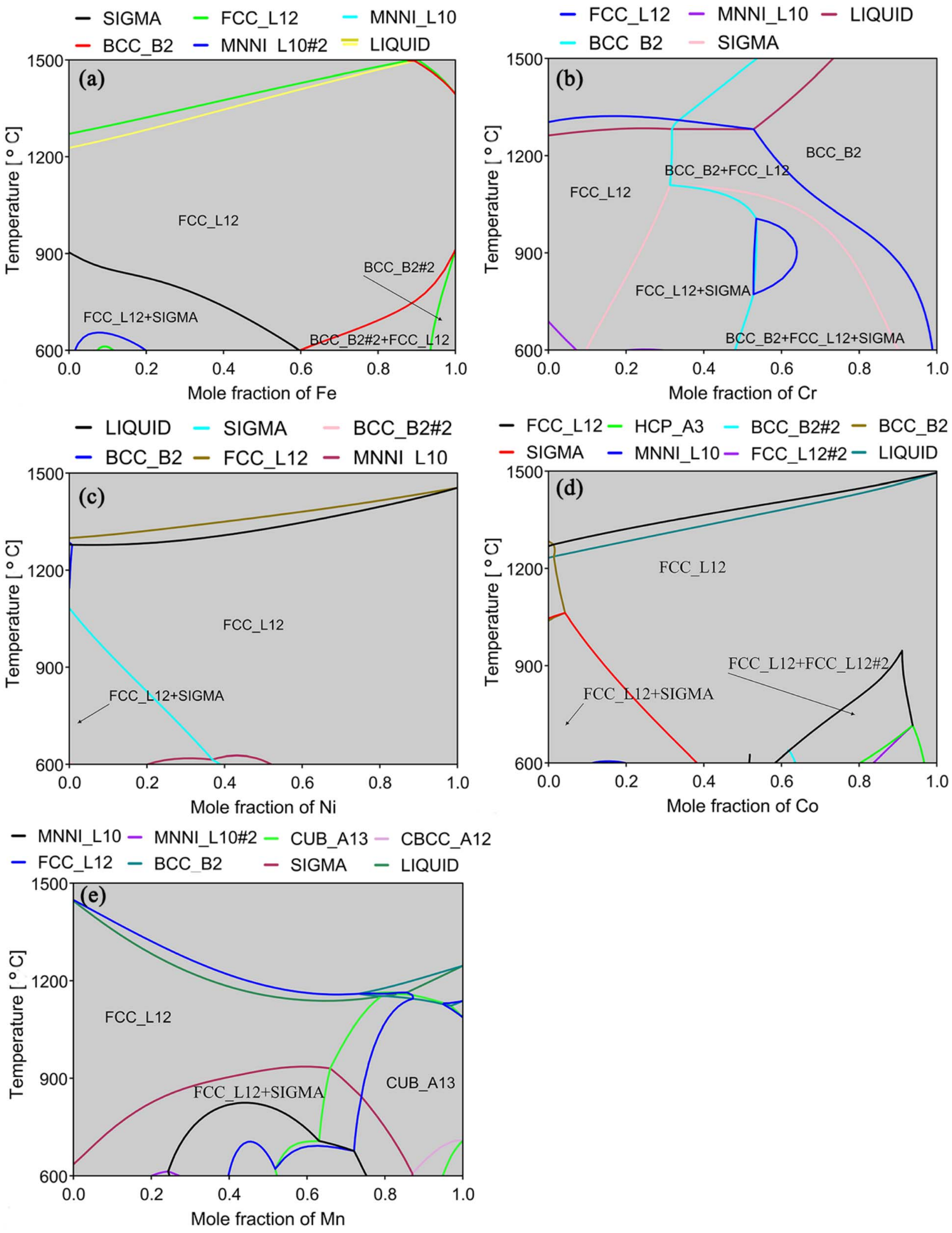

Fig. 14 Phase diagrams of FeCrNiCoMn system: (a) $Fe_x(CrNiCoMn)_{1-x}$, (b) $Cr_x(FeNiCoMn)_{1-x}$, (c) $Ni_x(FeCrCoMn)_{1-x}$, (d) $Co_x(FeCrNiMn)_{1-x}$, and (e) $Mn_x(FeCrNiCo)_{1-x}$.

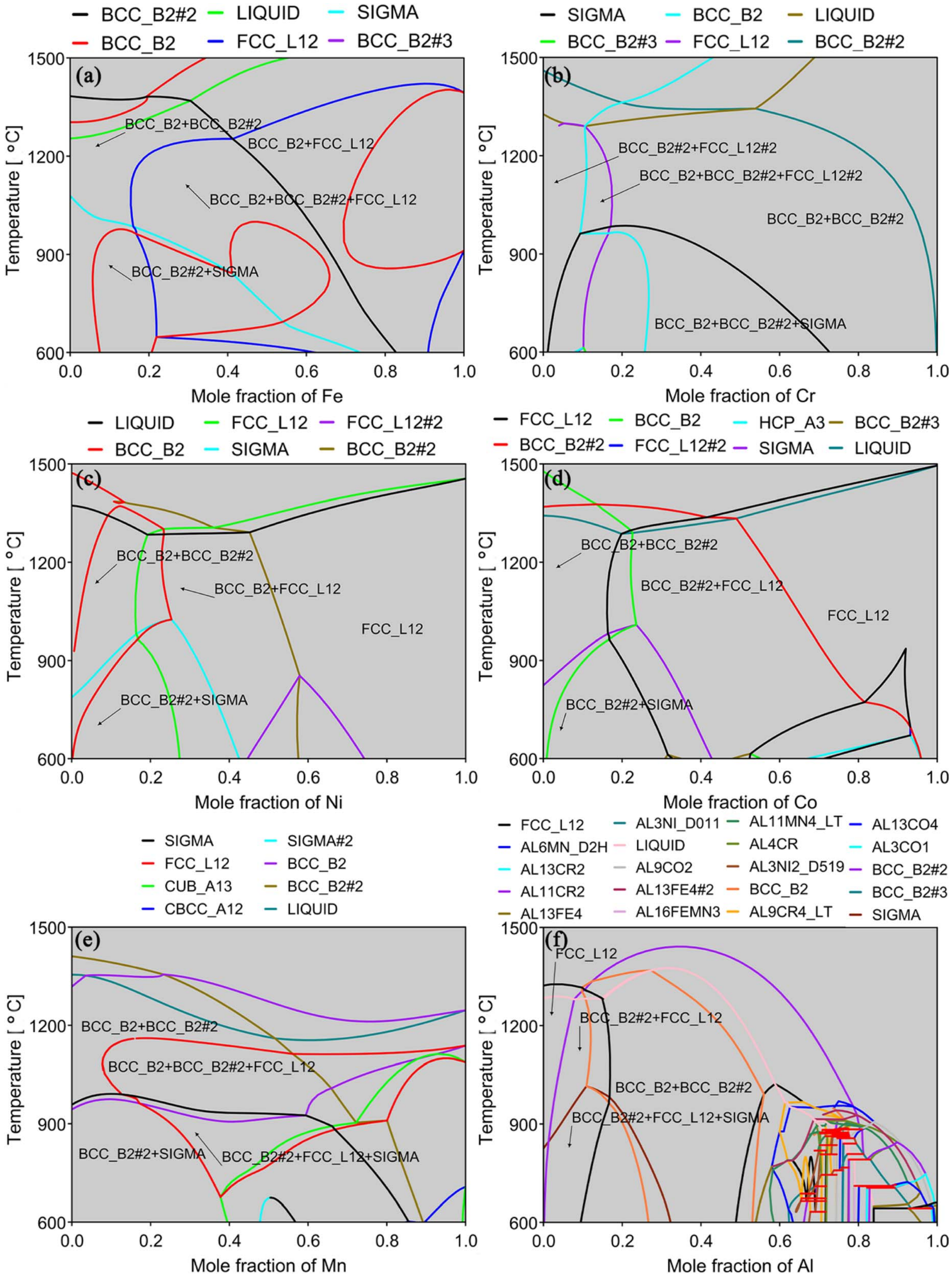

Fig. 15 Phase diagrams of FeCrNiCoMnAl system: (a) $Fe_x(CrNiCoMnAl)_{1-x}$, (b) $Cr_x(FeNiCoMnAl)_{1-x}$, (c) $Ni_x(FeCrCoMnAl)_{1-x}$, (d) $Co_x(FeCrNiMnAl)_{1-x}$, (e) $Mn_x(FeCrNiCoAl)_{1-x}$, and (f) $Al_x(FeCrNiCoMn)_{1-x}$.

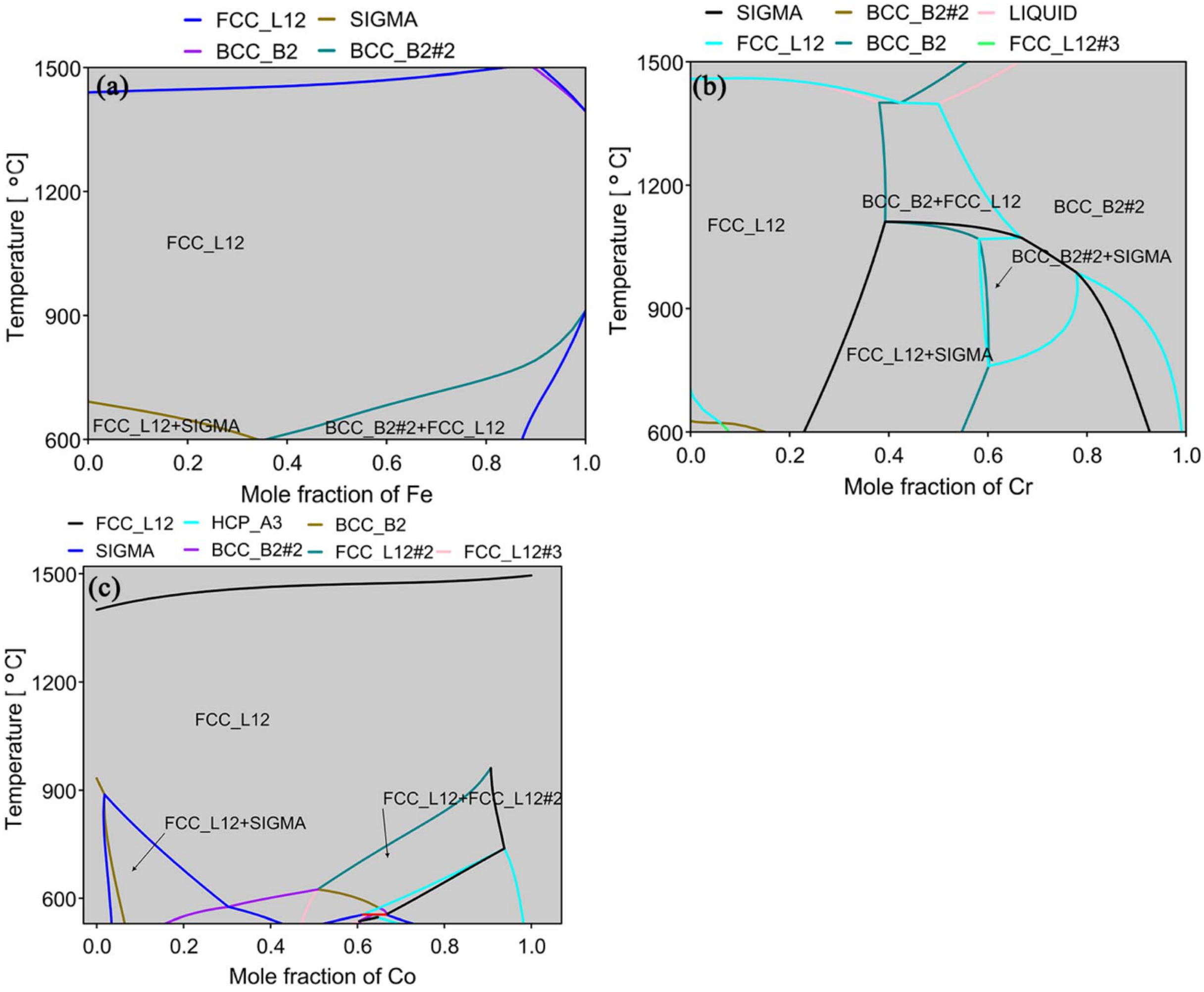

Fig. 16 Phase diagrams of FeCrNiCo system: (a) $Fe_x(CrNiCo)_{1-x}$, (b) $Cr_x(FeNiCo)_{1-x}$, and (c) $Co_x(FeCrNi)_{1-x}$.

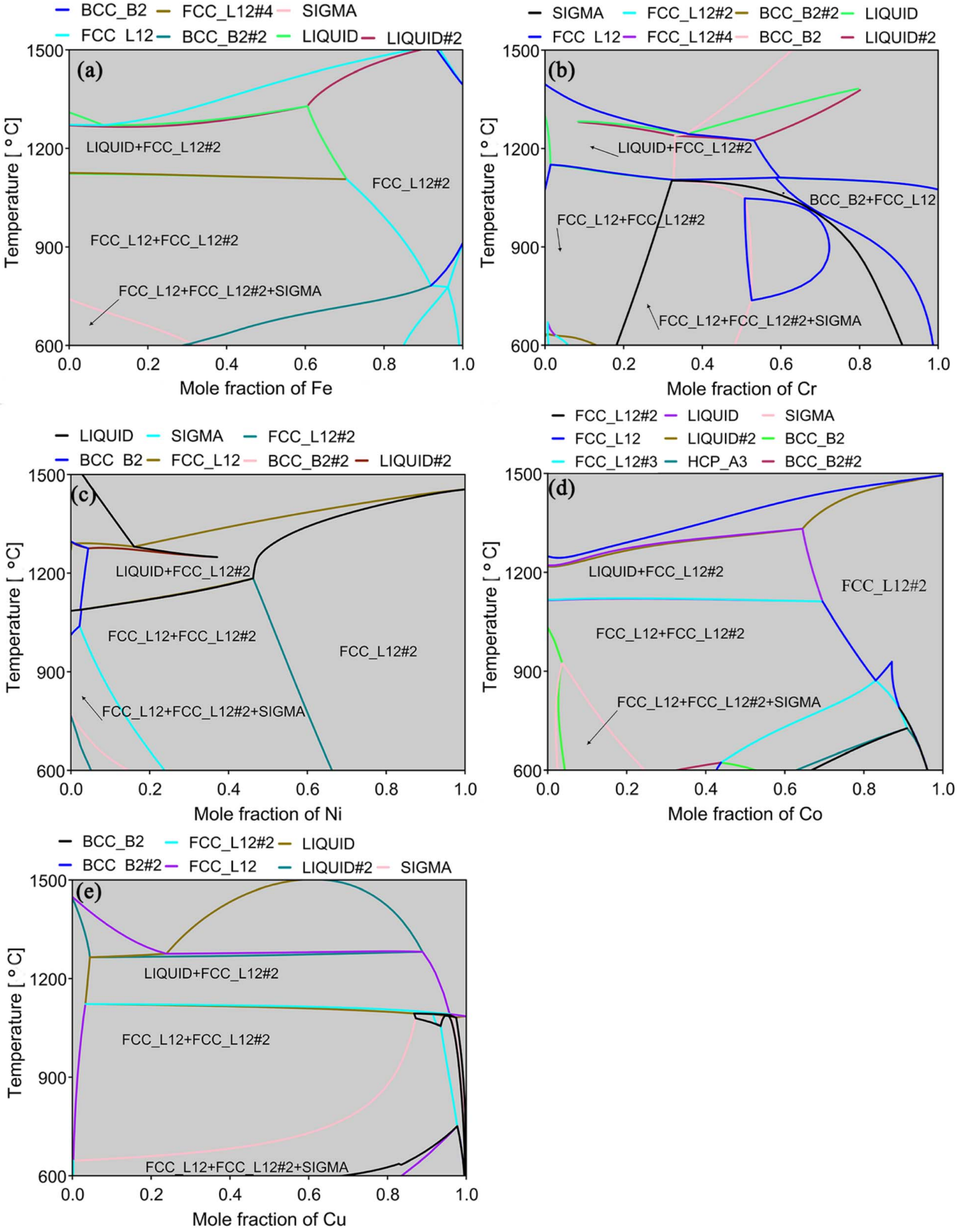

Fig. 17 Phase diagrams of FeCrNiCoCu system: (a) $Fe_x(CrNiCoCu)_{1-x}$, (b) $Cr_x(FeNiCoCu)_{1-x}$, (c) $Ni_x(FeCrCoCu)_{1-x}$, (d) $Co_x(FeCrNiCu)_{1-x}$, and (e) $Cu_x(FeCrNiCo)_{1-x}$.

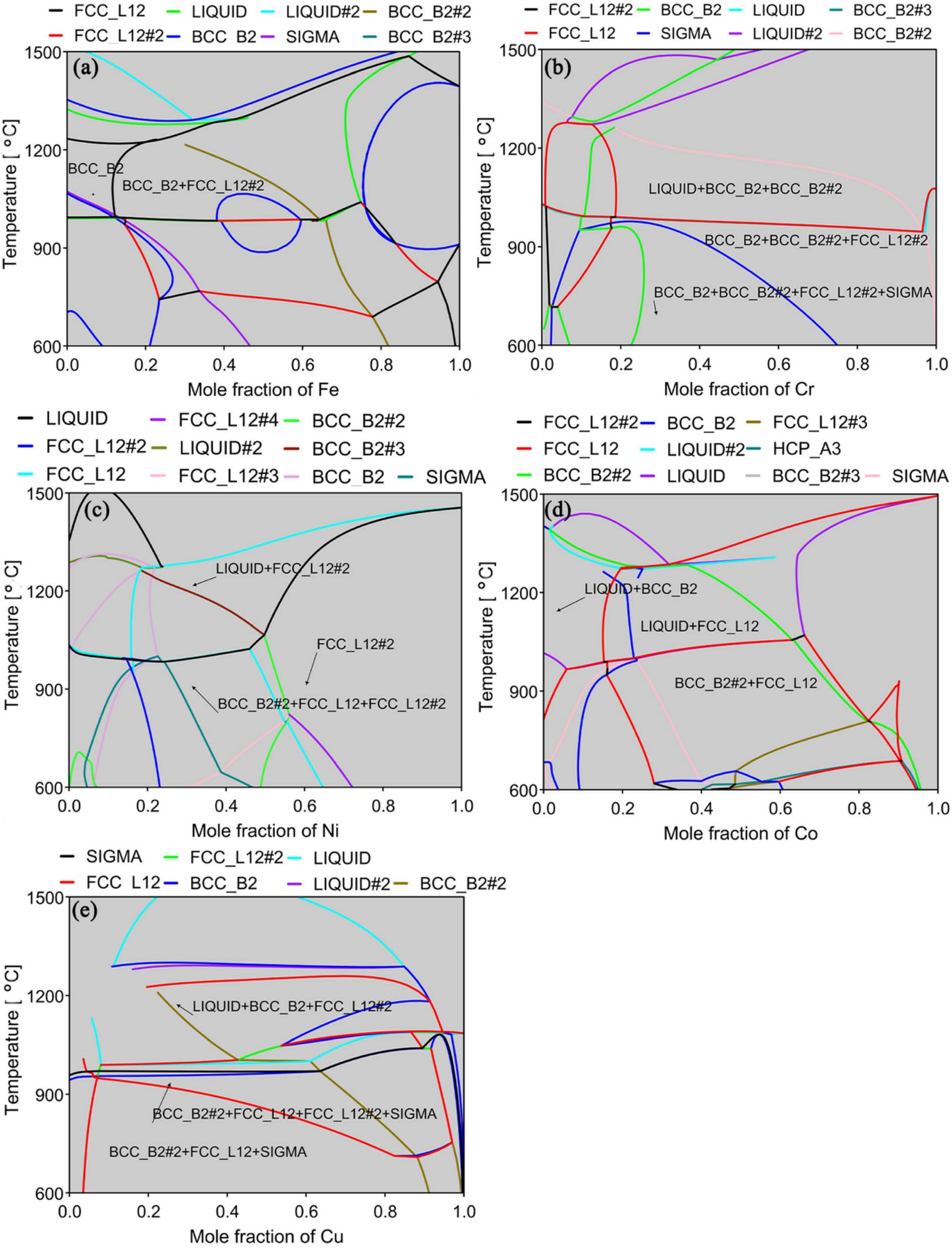

Fig. 18 Phase diagrams of FeCrNiCoCuAl system: (a) $Fe_x(CrNiCoCuAl)_{1-x}$, (b) $Cr_x(FeNiCoCuAl)_{1-x}$, (c) $Ni_x(FeCrCoCuAl)_{1-x}$, (d) $Co_x(FeCrNiCuAl)_{1-x}$, and (e) $Cu_x(FeCrNiCoAl)_{1-x}$.

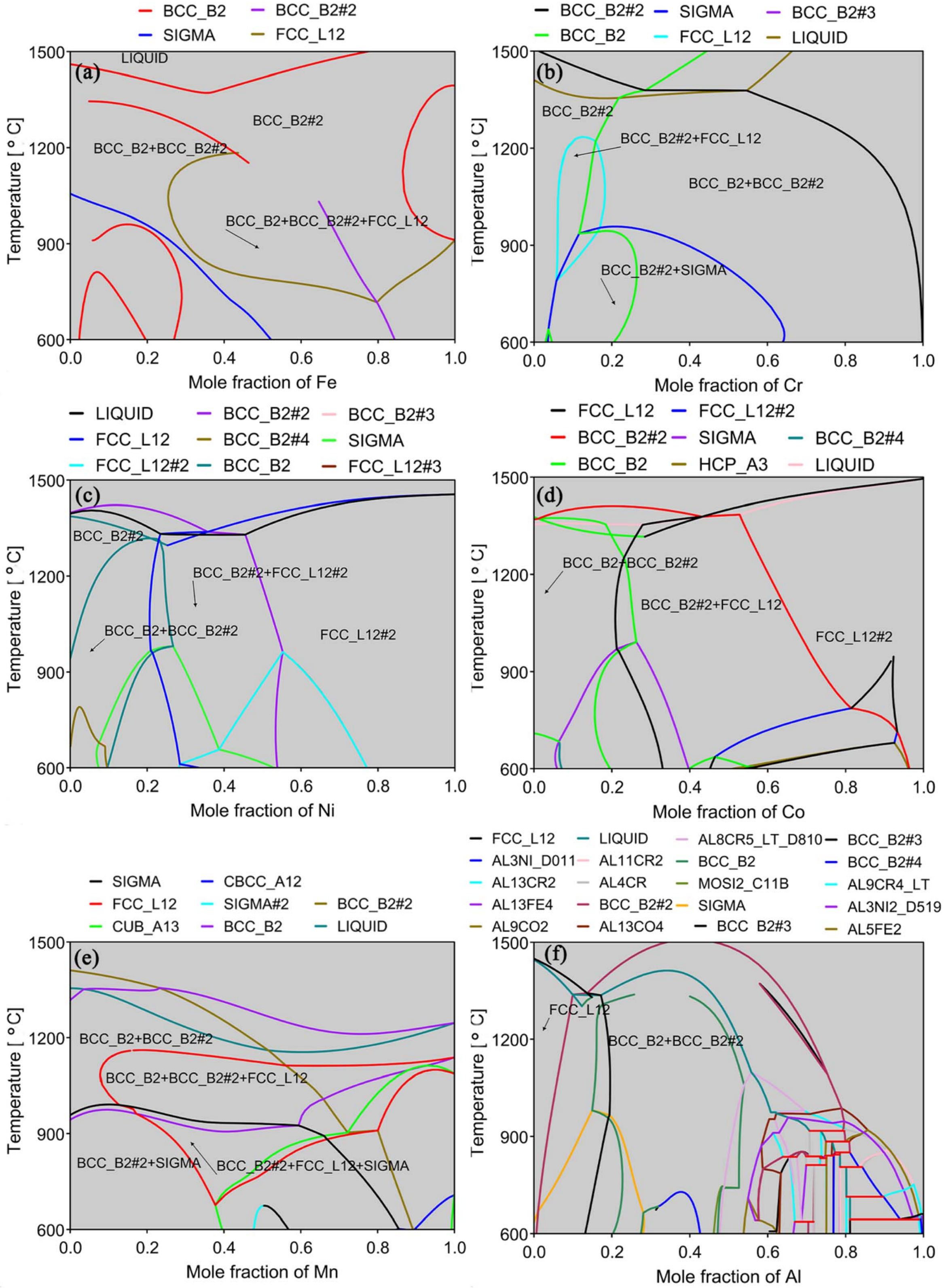

Fig. 19 Phase diagrams of FeCrNiCoAl system: (a) $Fe_x(CrNiCoAl)_{1-x}$, (b) $Cr_x(FeNiCoAl)_{1-x}$, (c) $Ni_x(FeCrCoAl)_{1-x}$, (d) $Co_x(FeCrNiAl)_{1-x}$, (e) $Mn_x(FeCrNiCo)_{1-x}$, and (f) $Al_x(FeCrNiCo)_{1-x}$.

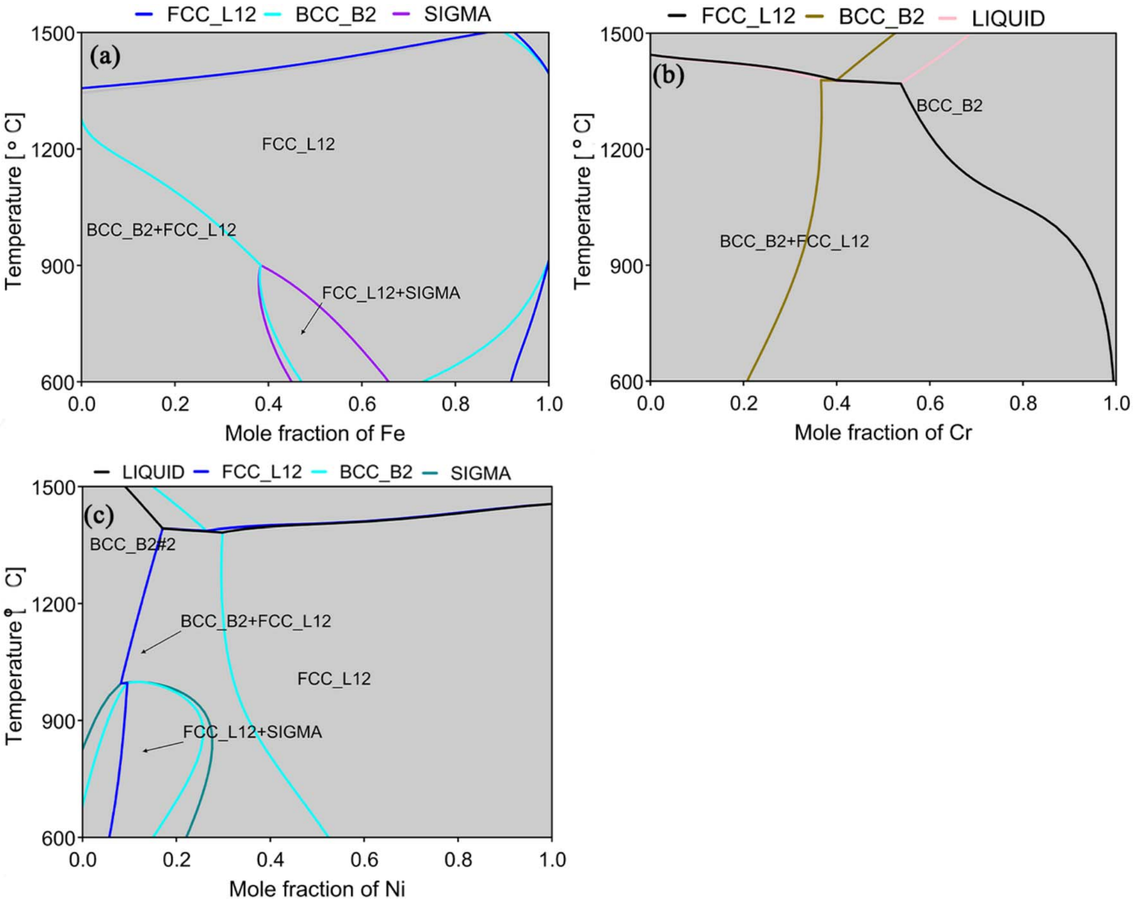

Fig. 20 Phase diagrams of FeCrNi system: (a) $Fe_x(CrNi)_{1-x}$, (b) $Cr_x(FeNi)_{1-x}$, and (c) $Ni_x(FeCr)_{1-x}$.

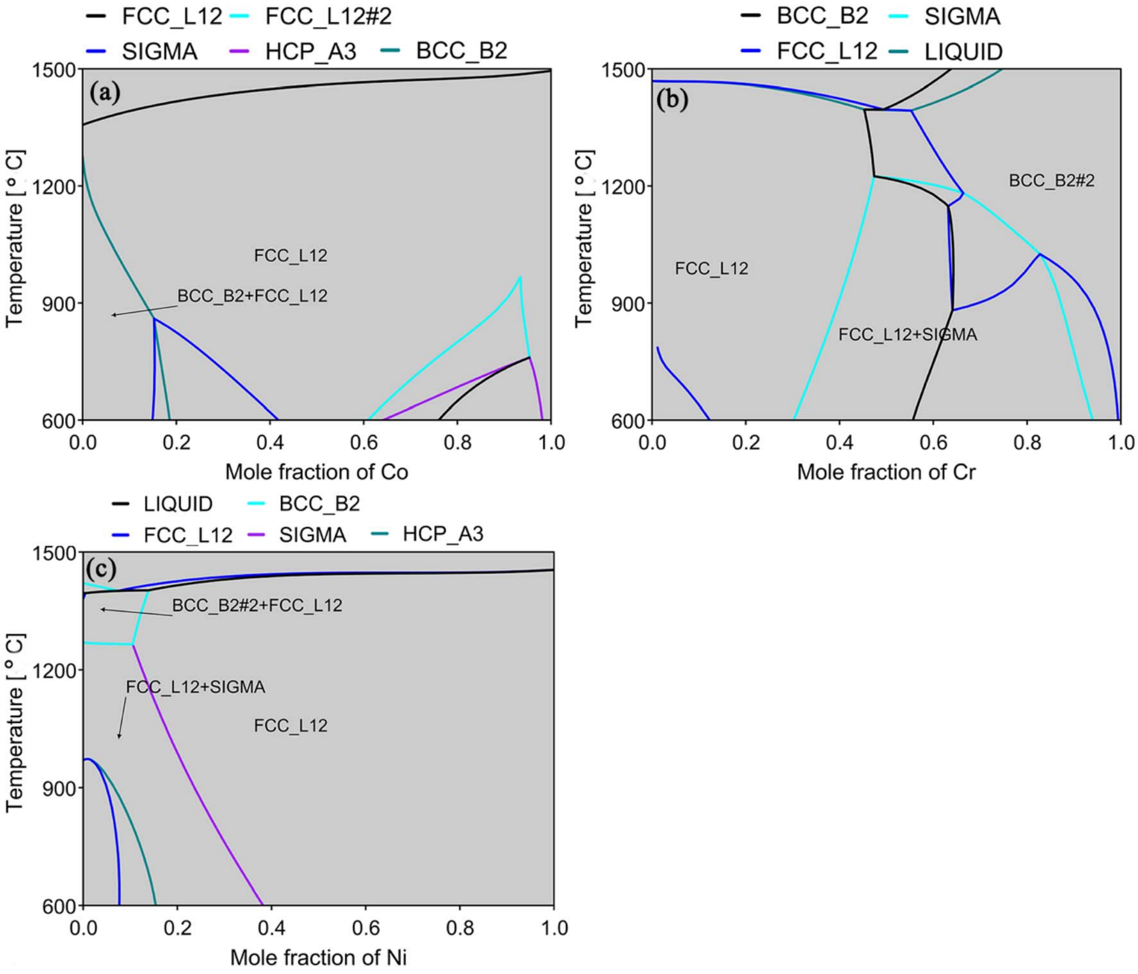

Fig. 21 Phase diagrams of CoCrNi system: (a) $Co_x(CrNi)_{1-x}$, (b) $Cr_x(CoNi)_{1-x}$, and (c) $Ni_x(CoCr)_{1-x}$.

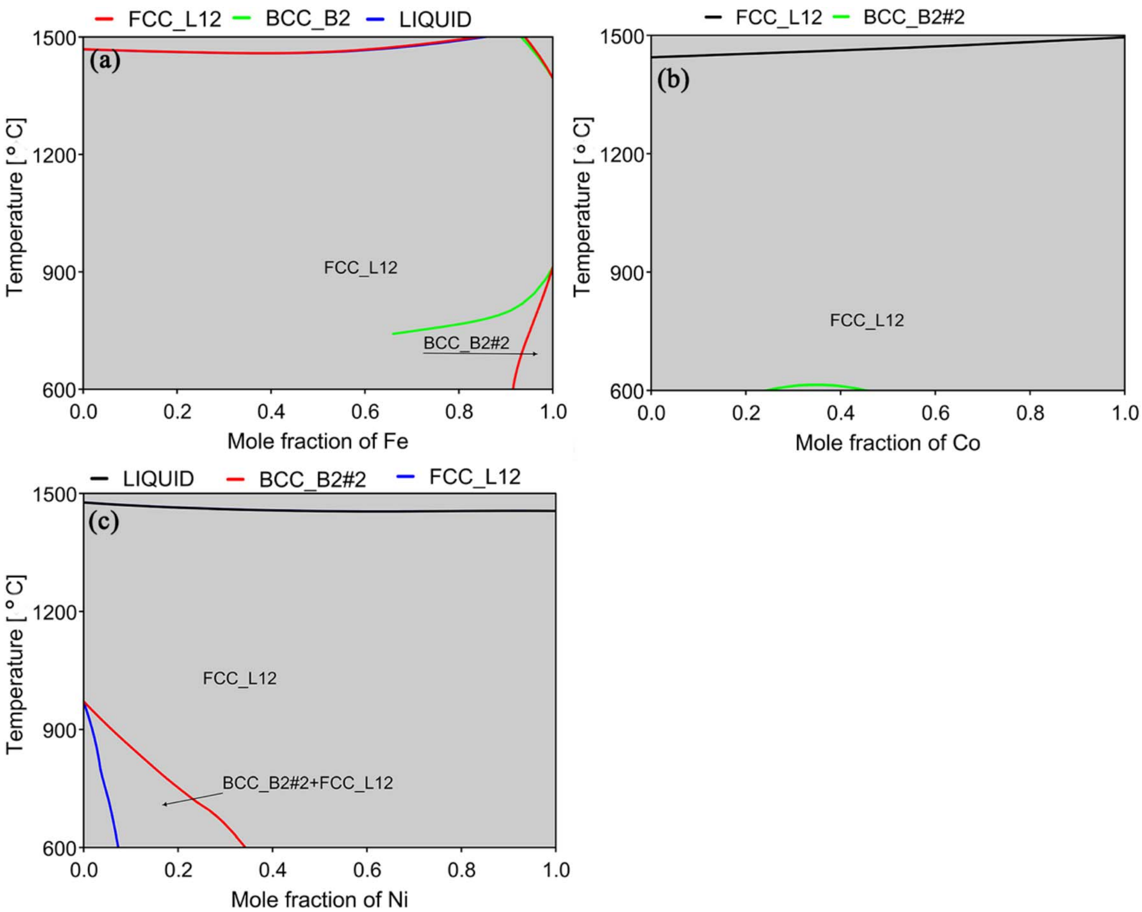

Fig. 22 Phase diagrams of FeCoNi system: (a) $Fe_x(CoNi)_{1-x}$, (b) $Co_x(FeNi)_{1-x}$, and (c) $Ni_x(FeCo)_{1-x}$.

Acknowledgements

The authors would like to acknowledge the financial support of the research seed funding from the CME Department at the University of Alberta.

References

1 A. Escamilla, D. Sánchez and L. García-Rodríguez, *Int. J. Hydrogen Energy*, 2022, **47**, 17505–17525.
2 M. Li, H. Zhang, Y. Zeng and J. Liu, *Acta Mater.*, 2022, **239**, 118267.
3 J. Chen, X. Zhou, W. Wang, B. Liu, Y. Lv, W. Yang, D. Xu and Y. Liu, *J. Alloys Compd.*, 2018, **760**, 15–30.
4 D. B. Adler, A. Jha and E. Severnini, *Resour. Energy Econ.*, 2020, **59**, 101127.
5 A. Khosravi, V. Olkkonen, A. Farsaei and S. Syri, *Energy*, 2020, **203**, 117884.
6 X. Du, X. Ma, J. Liu, S. Wu and P. Wang, *Nucl. Eng. Technol.*, 2022, **54**, 2840–2851.
7 A. Pineau and S. D. Antolovich, *Eng. Failure Anal.*, 2009, **16**, 2668–2697.
8 S. Manigandan, A. E. Atabani, V. K. Ponnusamy and P. Gunasekar, *Fuel*, 2020, **276**, 118104.
9 O. Balli and H. Caliskan, *Energy*, 2021, **232**, 121031.
10 P. C. Gasson, *J. Aeronaut. Sci.*, 2008, **112**, 291.
11 D. Furrer and H. Fecht, *JOM*, 1999, **51**, 14–17.
12 D. B. Miracle and O. N. Senkov, *Acta Mater.*, 2017, **122**, 448–511.
13 L. E. Geambazu, I. Voiculescu, C. A. Manea and R. V. Bololoi, *Appl. Sci.*, 2022, **12**, 7196.
14 X. Fu, C. A. Schuh and E. A. Olivetti, *Scr. Mater.*, 2017, **138**, 145–150.
15 B. Cantor, I. T. H. Chang, P. Knight and A. J. B. Vincent, *Mater. Sci. Eng., A*, 2004, **375–377**, 213–218.
16 J. W. Yeh, S. K. Chen, S. J. Lin, J. Y. Gan, T. S. Chin, T. T. Shun, C. H. Tsau and S. Y. Chang, *Adv. Eng. Mater.*, 2004, **6**, 299–303.
17 H. Luo, S. Zou, Y. Chen, Z. Li, C. Du and X. Li, *Corros. Sci.*, 2020, **163**, 108287.
18 W. Wang, W. Wang, S. Wang, Y. Tsai, C. Lai and J. Yeh, *Intermetallics*, 2012, **26**, 44–51.
19 Q. Zhou, S. Sheikh, P. Ou, D. Chen, Q. Hu and S. Guo, *Electrochem. Commun.*, 2019, **98**, 63–68.
20 F. Liu, P. K. Liaw and Y. Zhang, *Metals*, 2022, **12**, 501.
21 Y. J. Zhao, J. W. Qiao, S. G. Ma, M. C. Gao, H. J. Yang, M. W. Chen and Y. Zhang, *Mater. Des.*, 2016, **96**, 10–15.
22 Y. Yamabe-Mitarai, K. Yanao, Y. Toda, I. Ohnuma and T. Matsunaga, *J. Alloys Compd.*, 2022, **911**, 164849.

23 Z. Li, K. G. Pradeep, Y. Deng, D. Raabe and C. C. Tasan, *Nature*, 2016, **534**, 227–230.

24 F. Zheng, G. Zhang, X. Chen, X. Yang, Z. Yang, Y. Li and J. Li, *Mater. Sci. Eng., A*, 2020, **774**, 138940.

25 B. Schuh, F. Mendez-Martin, B. Völker, E. P. George, H. Clemens, R. Pippan and A. Hohenwarter, *Acta Mater.*, 2015, **96**, 258–268.

26 V. Dolique, A. L. Thomann, P. Brault, Y. Tessier and P. Gillon, *Surf. Coat. Technol.*, 2010, **204**, 1989–1992.

27 M. Esmaily, Y. Qiu, S. Bigdeli, M. B. Venkataraman, A. Allanore and N. Birbilis, *npj Mater. Degrad.*, 2020, **4**, 25.

28 A. Mohanty, J. K. Sampreeth, O. Bembalge, J. Y. Hascoet, S. Marya, R. J. Immanuel and S. K. Panigrahi, *Surf. Coat. Technol.*, 2019, **380**, 125028.

29 L. Li, J. Lu, X. Liu, T. Dong, X. Zhao, F. Yang and F. Guo, *Corros. Sci.*, 2021, **187**, 109479.

30 K. F. Quiambao, S. J. McDonnell, D. K. Schreiber, A. Y. Gerard, K. M. Freedy, P. Lu, J. E. Saal, G. S. Frankel and J. R. Scully, *Acta Mater.*, 2019, **164**, 362–376.

31 A. Mehta and Y. Sohn, *Diffus. Found.*, 2021, **29**, 75–93.

32 S. Sheikh, H. Mao and S. Guo, *J. Appl. Phys.*, 2017, **121**, 194903.

33 K. Kulkarni and G. P. S. Chauhan, *AIP Adv.*, 2015, **5**, 097162.

34 E. P. George, W. A. Curtin and C. C. Tasan, *Acta Mater.*, 2020, **188**, 435–474.

35 J. Joseph, N. Stanford, P. Hodgson and D. M. Fabijanic, *Scr. Mater.*, 2017, **129**, 30–34.

36 Z. Jiao, S. Ma, M. Chu, H. Yang, Z. Wang, Y. Zhang and J. Qiao, *J. Mater. Eng. Perform.*, 2016, **25**, 451–456.

37 H. Daoud, A. Manzoni, N. Wanderka and U. Glatzel, *JOM*, 2015, **67**, 2271–2277.

38 A. V. Kuznetsov, D. G. Shaysultanov, N. D. Stepanov, G. A. Salishchev and O. N. Senkov, *Mater. Sci. Eng., A*, 2012, **533**, 107–118.

39 D. Shaysultanov, G. Salishchev, Y. V. Ivanisenko, S. Zherebtsov, M. Tikhonovsky and N. Stepanov, *J. Alloys Compd.*, 2017, **705**, 756–763.

40 J.-l. Zhou, Y.-h. Cheng, Y.-x. Chen and X.-b. Liang, *Int. J. Refract. Met. Hard Mater.*, 2022, **105**, 105836.

41 N. K. Adomako, J. H. Kim and Y. T. Hyun, *J. Therm. Anal. Calorim.*, 2018, **133**, 13–26.

42 D. Huang, J. Lu, Y. Zhuang, C. Tian and Y. Li, *Corros. Sci.*, 2019, **158**, 108088.

43 G. Laplanche, U. F. Volkert, G. Eggeler and E. P. George, *Oxid. Met.*, 2016, **85**, 629–645.

44 W. Kai, C. C. Li, F. P. Cheng, K. P. Chu, R. T. Huang, L. W. Tsay and J. J. Kai, *Corros. Sci.*, 2017, **121**, 116–125.

45 M. P. Agustianingrum, F. H. Latief, N. Park and U. Lee, *Intermetallics*, 2020, **120**, 106757.

46 D. H. SPEIDEL and A. MUAN, *J. Am. Ceram. Soc.*, 1963, **46**, 577–578.

47 Y.-K. Kim, Y.-A. Joo, H. S. Kim and K.-A. Lee, *Intermetallics*, 2018, **98**, 45–53.

48 F. Ye, Z. Jiao, S. Yan, L. Guo, L. Feng and J. Yu, *Vacuum*, 2020, **174**, 109178.

49 Y. Cui, J. Shen, S. M. Manladan, K. Geng and S. Hu, *Appl. Surf. Sci.*, 2020, **512**, 145736.

50 R. Feng, M. C. Gao, C. Zhang, W. Guo, J. D. Poplawsky, F. Zhang, J. A. Hawk, J. C. Neuefeind, Y. Ren and P. K. Liaw, *Acta Mater.*, 2018, **146**, 280–293.

51 F. Otto, Y. Yang, H. Bei and E. P. George, *Acta Mater.*, 2013, **61**, 2628–2638.

52 G. Bracq, M. Laurent-Brocq, C. Varvenne, L. Perrière, W. A. Curtin, J. M. Joubert and I. Guillot, *Acta Mater.*, 2019, **177**, 266–279.

53 Y. Wei, Y. Fu, Z. Pan, Y. Ma, H. Cheng, Q. Zhao, H. Luo and X. Li, *Int. J. Miner., Metall. Mater.*, 2021, **28**, 915–930.

54 R. S. Roth, J. Dennis and H. McMurdie, *National Institute of Standards and Technology*, 1995, pp. 184–187.

55 A. Petric and H. Ling, *J. Am. Ceram. Soc.*, 2007, **90**, 1515–1520.

56 K. Y. Tsai, M. H. Tsai and J. W. Yeh, *Acta Mater.*, 2013, **61**, 4887–4897.

57 K.-M. Hsu, S.-H. Chen and C.-S. Lin, *Corros. Sci.*, 2021, **190**, 109694.

58 P. R. S. Jackson and G. R. Wallwork, *Oxid. Met.*, 1984, **21**, 135–170.

59 A. Ostovari Moghaddam, N. A. Shaburova, M. V. Sudarikov, S. N. Veselkov, O. V. Samoilova and E. A. Trofimov, *Vacuum*, 2021, **192**, 110412.

60 W. Kai, W. L. Jang, R. T. Huang, C. C. Lee, H. H. Hsieh and C. F. Du, *Oxid. Met.*, 2005, **63**, 169–192.

61 W. Kai, F. P. Cheng, Y. R. Lin, C. W. Chuang, R. T. Huang, D. Chen, J. J. Kai, C. T. Liu and C. J. Wang, *J. Alloys Compd.*, 2020, **836**, 155518.

62 J. Dąbrowa, G. Cieślak, M. Stygar, M. Zajusz, M. Jawańska, A. Gil, J. Jedliński, K. Mroczka, K. Matsuda, T. Kulik and M. Danielewski, *Oxid. Met.*, 2021, **96**, 307–321.

63 Q. C. Fan, B. S. Li and Y. Zhang, *J. Alloys Compd.*, 2014, **614**, 203–210.

64 Y. Song, L. Yan, X. Pang, Y. Su, L. Qiao and K. Gao, *Corros. Sci.*, 2023, **213**, 110983.

65 J. Dąbrowa, G. Cieślak, M. Stygar, K. Mroczka, K. Berent, T. Kulik and M. Danielewski, *Intermetallics*, 2017, **84**, 52–61.

66 M. Li, H. Zhang, Y. Zeng and J. Liu, *Acta Mater.*, 2022, **240**, 118313.

67 X. F. Wang, Y. Zhang, Y. Qiao and G. L. Chen, *Intermetallics*, 2007, **15**, 357–362.

68 D. J. Young, *High Temperature Oxidation and Corrosion of Metals*, Elsevier, 2008.

69 R. Wang, W. Chen, J. Zhong and L. Zhang, *J. Mater. Sci. Technol.*, 2018, **34**, 1791–1798.

70 J. Rebane, N. Yakovlev, D. Chicherin, L. Leonyuk and V. Yakunin, *J. Mater. Chem.*, 1997, **7**, 2085–2089.

71 A. C. S. Sabioni, A. M. Huntz, J. Philibert, B. Lesage and C. Monty, *J. Mater. Sci.*, 1992, **27**, 4782–4790.

72 Y. Y. Liu, Z. Chen, Y. Z. Chen, J. C. Shi, Z. Y. Wang, S. Wang and F. Liu, *Vacuum*, 2019, **169**, 108837.

73 T. M. Butler and M. L. Weaver, *J. Alloys Compd.*, 2016, **674**, 229–244.

74 T. M. Butler, J. P. Alfano, R. L. Martens and M. L. Weaver, *JOM*, 2015, **67**, 246–259.

75 L. Chen, Z. Zhou, Z. Tan, D. He, K. Bobzin, L. Zhao, M. Öte and T. Königstein, *J. Alloys Compd.*, 2018, **764**, 845–852.

76 M. Huang, J. Jiang, Y. Wang, Y. Liu and Y. Zhang, *Corros. Sci.*, 2021, **193**, 109897.
77 J. Zhu, S. Lu, Y. Jin, L. Xu, X. Xu, C. Yin and Y. Jia, *Oxid. Met.*, 2020, **94**, 265–281.
78 B. Li and B. Gleeson, *Oxid. Met.*, 2006, **65**, 101–122.
79 Y. Li, P. Zhang, J. Zhang, Z. Chen and B. Shen, *Corros. Sci.*, 2021, **190**, 109633.
80 W. Kai, F. P. Cheng, C. Y. Liao, C. C. Li, R. T. Huang and J. J. Kai, *Mater. Chem. Phys.*, 2018, **210**, 362–369.
81 N. Liu, M. Xu, Y. Y. Qian and P. J. Zhou, *J. Alloys Compd.*, 2021, **870**, 159320.
82 G.-S. Ham, Y.-K. Kim, Y. S. Na and K.-A. Lee, *Met. Mater. Int.*, 2021, **27**, 156–165.
83 S. Jiang, Z. Lin, H. Xu and Y. Sun, *J. Alloys Compd.*, 2018, **741**, 826–833.
84 Y.-J. Chang and A.-C. Yeh, *J. Alloys Compd.*, 2015, **653**, 379–385.
85 S. Wang, Z. Chen, P. Zhang, K. Zhang, C. L. Chen and B. L. Shen, *Vacuum*, 2019, **163**, 263–268.
86 H. Sun, M. Li, H. Zhang and J. Liu, *Corros. Sci.*, 2024, **227**, 111685.
87 Y. Xie, C. Wang, K. Zhang, C. Liang, M. Liang, W. Liu and J. Yang, *Vacuum*, 2021, **191**, 110364.
88 M. P. Agustianingrum, U. Lee and N. Park, *Corros. Sci.*, 2020, **173**, 108755.
89 Z. Peng, J. Sun, H. Luan, N. Chen and K. Yao, *Intermetallics*, 2023, **155**, 107845.
90 M. Li, H. Henein, C. Zhou and J. Liu, *J. Mater. Sci. Technol.*, 2024, **174**, 133–144.
91 M. Li, H. Sun, X. Tan, H. Zhang and J. Liu, *Mater. Today*, 2024, **74**, 46–57.
92 S. Guo and C. T. Liu, *Prog. Nat. Sci.: Mater. Int.*, 2011, **21**, 433–446.
93 A. Takeuchi and A. Inoue, *Mater. Trans.*, 2005, **46**, 2817–2829.
94 R. Li, L. Xie, W. Y. Wang, P. K. Liaw and Y. Zhang, *Front. Mater. Sci.*, 2020, **7**, 290.
95 S. Mooraj and W. Chen, *J. Mater. Inf.*, 2023, **3**, 4.
96 H. Sun, C. He and J. Liu, *Presented in Part at the AMPP Annual Conference*, New Orleans, US, 2024.
97 H. Sun and J. Liu, *Eng. Failure Anal.*, 2022, **133**, 105964.
98 H. Sun, L. Sun, T. Du, J. Wang and J. Liu, *Conference of Metallurgists*, 2021.
99 N. J. van Eck and L. Waltman, *Scientometrics*, 2010, **84**, 523–538.
100 C. Wen, Y. Zhang, C. Wang, D. Xue, Y. Bai, S. Antonov, L. Dai, T. Lookman and Y. Su, *Acta Mater.*, 2019, **170**, 109–117.
101 X. Liu, J. Zhang and Z. Pei, *Prog. Mater. Sci.*, 2023, **131**, 101018.
102 W. Huang, P. Martin and H. L. Zhuang, *Acta Mater.*, 2019, **169**, 225–236.
103 Y.-G. Yan, D. Lu and K. Wang, *Tungsten*, 2023, **5**, 32–49.
104 S. Hou, Y. Li, M. Bai, M. Sun, W. Liu, C. Wang, H. Tetik and D. Lin, *Materials*, 2022, **15**, 3321.
105 Y. Zhang, C. Wen, C. Wang, S. Antonov, D. Xue, Y. Bai and Y. Su, *Acta Mater.*, 2020, **185**, 528–539.
106 S. Abbaszadeh, A. Pakseresht, H. Omidvar and A. Shafiei, *Surf. Interfaces*, 2020, **21**, 100724.
107 R. Gawel, Ł. Rogal, J. Dąbek, M. Wójcik-Bania and K. Przybylski, *Vacuum*, 2021, **184**, 109969.
108 Y. Garip, N. Ergin and O. Ozdemir, *J. Alloys Compd.*, 2021, **877**, 160180.
109 S. Kumar T, A. Sourav, B. S. Murty, A. Chelvane and S. Thangaraju, *J. Alloys Compd.*, 2022, **919**, 165820.
110 J. Lu, Y. Chen, H. Zhang, N. Ni, L. Li, L. He, R. Mu, X. Zhao and F. Guo, *Corros. Sci.*, 2020, **166**, 108426.
111 C. Zhang, M. Zheng, M. Zhu, L. Yao and Z. Jian, *J. Mater. Eng. Perform.*, 2023, **32**, 8100–8110.
112 L. Liu, S. Wu, Y. Dong and S. Lü, *Corros. Sci.*, 2016, **104**, 236–247.
113 F. Chang, B. Cai, C. Zhang, B. Huang, S. Li and P. Dai, *Surf. Coat. Technol.*, 2019, **359**, 132–140.
114 Y. Zhang, H. Wu, X. Yu and D. Tang, *Corros. Sci.*, 2022, **200**, 110211.